Politecnico di Milano

Corso di laurea in *Materials engineering and Nanotechnology*
Scuola di ingegneria industriale e dell'informazione

Direct synthesis of *MoS*$_2$ on Silicon by atmospheric pressure CVD as catalyst for hydrogen generation

Supervisor: Prof. Andrea Li Bassi
                 Politecnico di Milano
Supervisor: Prof. Anna Fontcuberta I Morral
                 École polytechnique fédérale de Lausanne
Co-supervisor: Esther Alarcon Llado
                 École polytechnique fédérale de Lausanne

Author:
Luca Del Carro   Matr. 814683

Academic Year 2014-2015

From the book written by Jules Verne in 1874 *The Mysterious Island*:

"Yes, my friends, I believe that water will one day serve as our fuel, that the hydrogen and oxygen which compose it, used alone or together, will supply an inexhaustible source of heat and light, burning with an intensity that coal cannot equal. One day, in the place of coal, the coal bunkers of steamers and the tenders of locomotives will be loaded with these two compressed gases which will burn in furnaces with an enormous heating power. I believe that when the coal mines have been exhausted, we will both heat and be heated with water. *Water is the coal of the future."*

Abstract

In recent years, layered transition metal chalcogenides (MX_2) have attracted a great attention due to their unique combinations of optical [33] , electrical [30, 38] and chemical properties [3] when confined in $2D$ structures. In particular nanostructured molibdenite, which exhibits a direct band gap of $1.8eV$ for a single molecular layer, has emerged as a promising catalyst due to its lower cost and earth-abundant. More recently, it has been shown by a combination of electrochemistry and surface science, that only the edge sites of nanostructured MoS_2 are catalytically active for hydrogen evolution: this localised activity is thought to be due to the presence of under-coordinated sulphur atoms. Such edges exhibit a metallic character that leads to a more effective adsorption of H^+ ions and following reduction to H_2 molecule [23, 8]. Indeed many efforts have been made, both with top down and bottom up approaches [24, 9, 37] , to obtain a catalyst morphology which shows a large amount of edges, in order to improve HER kinetics. In this work we present a novel study and modulation of $2D$ MoS_2 based vertically aligned nanostructure growth, called *nanoflakes*, directly performed on different substrates of p-type silicon by atmospheric pressure chemical vapour deposition. Our results clearly show a new way to control morphology of MoS_2 grown nanostructure .

We demonstrate a decrease of HER overpotential after the application of MoS_2 nanoflakes.

This new design suggests an enhanced applicability of 2D MoS2 vertically aligned nanoflakes as catalyst for hydrogen evolution reaction, in PEC device based on Si.

Abstract

Negli ultimi anni i metalli dicalcogenati (MX_2) hanno suscitato grande interesse nella comunit*á* scientifica per via delle loro straordinarie proprietà ottiche, elettriche e chimiche esibite se confinati in strutture $2D$. In particolare la molibdenite nanostrutturata (MoS_2) *é* stata individuata come potenziale catalizzatore rivoluzionario per la produzione di idrogeno sia per la sua comprovata attivit*á* che per la sua elevata disponibilit*á* in natura e basso costo. Studi recenti hanno dimostrato che solo i siti laterali della MoS_2 nanostrutturata sono attivi nel catalizzare l'evoluzione di idrogeno. Tale attivit*á* localizzata *é* dovuta alla presenza alle estremit*á* di atomi di zolfo non coordinati. Tali atomi aumentano l'efficienza di assorbimento di ioni H^+ e di conseguenza ottimizzano la cinetica di riduzione di tali ioni a H_2 molecolare. Per questi motivi, molti sforzi sono stati recentemente fatti per sintetizzare un catalizzatore con una forma tale da esporre il maggior numero possibile di siti laterali attivi direttamente a contatto con l'elettrolita (il quale contiene gli ioni H^+).

In questo lavoro presento un nuovo metodo di crescita della MoS_2 $2D$ nanostrutturata verticalmente allineata al substrato di crescita. Tali strutture, chiamate *nanoflakes*, sono state sintetizzate tramite atmospheric pressure chemical vapour deposition su diversi substrati si silicio, ovvero con diversa direzione cristallografica (<111> e <100>) e diversa struttura (da silicio planare ad array di nano e micro pillars). I risultati riportati mostrano un controllo estremamente riproducibile della morfologia di crescita della MoS_2, la quale cambia direzione di orientamento rispetto al substrato da orizzontale a verticale al variare dei parametri di sintesi selezionati. Durante lo studio della crescita *é* emerso che la massima temperatura di deposizione raggiunta nella camera durante il processo *é* il parametro che domina questa transizione dell'allineamento. Nel corso del lavoro sono stati studianti gli effetti di tutti gli altri parametri modificabili nel processo di sintesi, ovvero : il tempo di processo alla massima temperatura, la temperatura di entrata dei precursori gassosi e la quantit*á* e rapporto fra i precursori gassosi. Le strutture sintetizzate con le differenti ricette di deposizione sono state metodicamente caratterizzate con :Raman spectroscopy, Photoluminescence, x-ray diffraction, SEM e TEM.

Secondariamente *é* stato studiato l'effetto di un processo di sulfurizzazione a posteriori sulla struttura e composizione chimica dei nanoflakes.

Infine per ogni differente tipo di campione *é* stata testata l'effettiva efficienza nel catalizzare la riduzione d'idrogeno. I risultati riportati in questo testo mostrano un effettiva catalisi della reazione di evoluzione dell'idrogeno promossa da alcuni tipi di MoS_2 da noi sintetizzata.

Acknowledgments

First of all I would like to thank Prof. Anna Fontcuberta I Morral for the possibility to joint her group both for a summer internship and my master project. Her constant scientific, human and economical support helped me in growing up as engineer and man during this wonderful experience.

I can't find proper words to thank my mentor in LMSC : Dr. Esther Alarcon Llando. She was constantly present during all my work, ready to help me in all the steps of the project and to share with me her experience in the field. It was a great honor and pleasure for me to work with a such prepared and valuable scientist.

I would like to thank all my colleagues in LMSC for all the great moments spent together during these months. I would like to start thanking my lab-mate Eleonora Frau for all the proficient discussions and her infinite patience and kindness. Francesca Amaduzzi, for the help in Raman experiments and to be always ready to listen me. Luca Francaviglia and Martin Friedl for all the fun, the activities and the great moments spent together. Jelena Vukajlovic Plestina for all her help in the clean-room and for have prepared pillar arrays for me. Heidi Potts for all her help in the clean-room . Dmitry Mikulik for the proficient discussions and the great football matches. Federico Matteini and Alberto Casadei for the wonderful hiking trips. Jean-Baptiste Leran to organize the football matches. Yannik Fontana for his help with Raman set-up and for his positive mood. Gozde Tutuncuoglu to be always kind and super positive. Monika for his precious work and to all the good suggestions.

Moreover I would like to thank Prof Andras Kis to give me access to LANES facilities and Dr. Dumitru Dumcenco for his fundamental help in using AP-CVD. I'm very grateful to Dr. Arnaud Magrez for his help with XRD set-up and to whole CMI and ICMP staffs.

A special thank goes to my supervisor Prof. Andrea Li Bassi for his constant presence and availability during my master project.

Inoltre ringrazio di cuore tutta la mia famiglia e Anna per il loro sostegno e affetto durante questa esperienza. Infine ringrazio i miei amici e colleghi Francesco, Stefano,Elena, Riccardo, Jacopo e Giorgio per l'aiuto, il sostegno e la loro amicizia durante questi anni di studio nell nostro Politecnico.

Contents

List of Figures

Chapter 1

Introduction

Energy demand satisfaction is the greatest and highest compelling problem to solve in the near future. The exponential increase of energy consumption and the rapid empty of fossil fuel reservoirs lead to the necessity to find an alternative clean, storable and readily available energy form.

In this sense,clean energy can be obtained by capturing and converting solar light into usable energy. The Sun is a gigantic source of energy providing the Earth with about $3 * 10^{24}$ joules a year. The transformation of solar energy into electricity has fascinated researchers and engineers since the French scientist Edmond Becquerel discovered the photoelectric effect, creating the forefather of the actual photovoltaics (PV) devices [5].

In contrast, solar fuels represent the ultimate goal in the field of energy generation because it converts sunlight directly into a stable chemical bond, creating a fuel that can be easily transported and stored to be used upon demand. The first of solar to fuel conversion is the spontaneous electrolysis of water upon illumination, to store solar energy in the simplest chemical bond: H_2.

The H_2 molecule is an ideal fuel because:

- It has an high energy value: it can store 3 times the energy per unit mass as gasoline and 7 times as coal one (being able to release $142 MJ/kg$ during combustion);

- It can be produced from and converted into electricity at relatively high efficiencies;

- It can be produced using water as raw material;

- It can be stored in molecular gas phase;

- It can be transported for long distances using pipelines, which are less expensive that conductive cables;

- It is environmentally friendly because storage and utilization methods does not produce pollutants ;

- It can be used to feedstock fuel cells and all other devises that currently run with natural gas injection.

Hydrogen is not only used directly as fuel, but in other industries. Approximately half of this hydrogen goes to making ammonia (NH_3), which is a major component of fertilizer and a familiar ingredient in household cleaners. Approximately 37% of the hydrogen is used in refineries for chemical processes such as removing sulphur from gasoline and converting heavy hydrocarbons into gasoline and diesel fuel. The remaining hydrogen is used for applications including edible fat hydrogenation, methanol production, float glass production, generator cooling, weather balloons and rockets.

Unfortunately, hydrogen is not readily available in nature and nowadays, the production costs are extremely high and not economically competitive with fossil fuels ones. This high cost mainly derives from the lack of an integrated system of production, which is able to directly convert a renewable energy source into molecular hydrogen avoiding intermediate steps of conversion from and to electricity, which lead to intrinsic dissipations.

Moreover, most of the current production methods involve chemical reactions with severe safety and environmental issues, based on the utilization of not renewable energy sources. In fact, since fossil fuel sources are currently abundant, they are used to produce about the 96% of the worlds' hydrogen, inside which natural gas covered the largest part, about 95%, being used in the "steam-methane reforming" (SMR) production method [20] .

In terms of numbers this means that 45 million metric tons of hydrogen are produced globally each year from fossil fuels.

It turns obvious that the aim of any realistic sustained energy system based on hydrogen necessitates the fabrication of hydrogen from clean sources, overcoming the issues of safety and environmental sustainability, to finally realise the so called *hydrogen economy* [11]. To reach such ambitious goal of an energy world demand satisfied only by clean hydrogen fuel (and the derivate electricity) we have to find a cost effective way, economically competitive, keeping in mind that a terawatt scale production is required .

Between all the possible methods of hydrogen generation by solar energy (thermolysis, thermochemical and biological conversion) [35], one of the most studied is photoelectrochemical (PEC) water splitting, where inorganic semiconductors are used to harvest sunlight and split water into H_2 and O_2.

PEC water splitting is an artificial process,which aims to emulate natural photosynthesis, where at least one of the two electrodes in contact with water is photoactive. The photoactive electrode must generate a voltage under sunlight irradiation which is used for the chemical reaction of water splitting.

In the following I introduce phototelectrochemical water splitting and its different key components.

1.1 Photoelectrochemical water splitting: how is possible to get it?

Water is a transparent colourless compound, fundamental for Life on our planet which is stable in liquid phase at ambient temperature and pressure. Due to this its stability in standard conditions, breaking the molecule's bond to produce H_2 and O_2 is not an easy task. In fact, a large quantity of energy must be provided.

But, how much does it "cost", in terms of energy, to split water?

From a thermodynamical point of view, a free energy difference of $\Delta G = 237, 2kJ/mol$ exists between a molecule of water and one of H_2 plus an atom of O. This energy corresponds to a potential absolute difference of $\Delta E = 1, 23V$ per transferred electron. There are two invloved reactions in water splitting:

$$H_2O + 2h^+ \rightarrow 1/2O_2 + 2H^+ \quad (HER) \tag{1.1}$$
$$2H^+ + 2e^- \rightarrow H_2 \quad (OER) \tag{1.2}$$
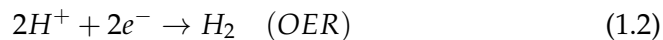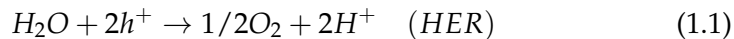
There are several methods to provide this energy to a water molecule. In this project, we are interested in using sunlight to drive photolysis. Water is transparent to visible light. As a consequence, this reaction cannot take place by only using the raw material (water). On that account, a semiconductor material can be used to mediate the reaction. The intrinsic properties of semiconductors and the nature of their junction with water enable the absorption of light and voltage generation.

The semiconductor material must be carefully selected. The chosen material must be able to absorb sunlight, while providing a photogenerated voltage larger than $1, 23V$. A detailed explanation on semiconductor-water junction is given in *Appendix A*. Also, charge transfer from the semiconductor to water must be considered since losses are induced by recombination phenomena.

Moreover, chemical reactions that will increase the potential needed (i.e. overpotential) and kinetic limitations are expected. In this regard, overpotentials are larger for semiconductor surfaces with respect to metallic ones,due to their poor catalytic properties.

As a consequence, a more realistic energy value that is often reported for the water photoelectrolysis is of $1, 6 - 2, 4eV$.

The first demonstration of solar water splitting was performed by Honda and Fujishima in 1972. With a brilliant intuition they demonstrated the
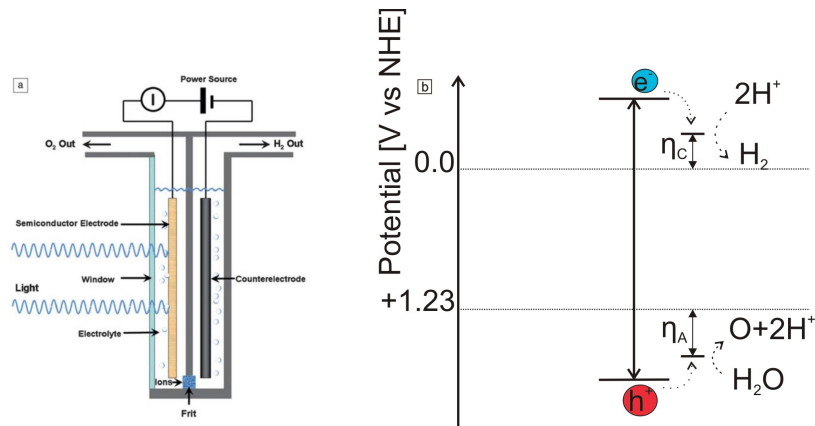
Figure 1.1: a) schematic representation of a single absorber based PEC cell. b) band scheme of a semiconductor material with a band gap large enough to achieve water splitting reaction. Figure used with author authorization [2]

possibility to split water by just using solar light as energy source and an n-type TiO_2 photoelectrode [17]. In this configuration, that is the simplest one, the PEC cell is formed by a photo-anode, made of an n-type semiconductor, and a metallic cathode. Indeed, all the required potential to achieve the water splitting reaction is provided by a single photoactive electrode. This implies that the band gap is large enough to provide the energy and the conduction band-edge energy (E_{cb}) and valence band-edge energy (E_{vb}) straddle the standard electrochemical potentials of hydrogen and oxygen evolution respectively [36].

Due to the large band gap of TiO_2, absorption is limited to ultraviolet region and low conversion efficiencies (about 2%) can be obtained [2]. Alternative oxides have been investigated, that can afford water splitting without any external bias and with a spectral response in the visible. However no outstanding efficiencies have been obtained so far [1].

Nowadays, multijunction configuration is preferred where two semiconductors with opposite doping type are connected in series in a so called *tandem cell*. In a tandem cell both electrodes are photoactive and each will be responsible for one half reaction: the photocathode to HER and the photoanode to OER.

Also in this case, two jointed counterparts have to provide the required potential keeping an overall band positions that straddle the oxygen and hydrogen standard potential values as reported in figure 1.2.
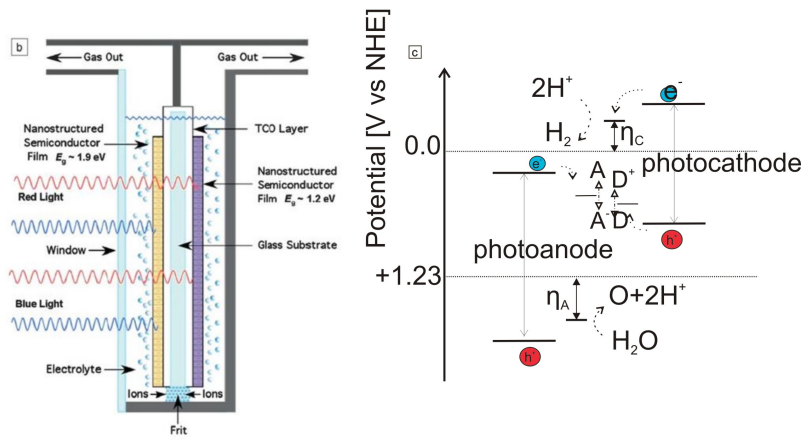
Figure 1.2: b) schematic representation of tandem PEC cell c) band scheme of two compatible semiconductor materials, able to carry out water splitting reaction. Figure used with author authorization [2]

As it is shown, the photoelectrodes are electronically connected together on one side and in contact with the electrolyte on the other.

It is possible to assess the overall solar to hydrogen efficiency (η_{STH}) of the device by characterizing the two photoelectrodes separately. The efficiency of a single photoelectrode can be computed from the current-voltage characteristics (I-V curve)as in photovoltaics. The maximum generated power and the fill factor values are parameters that assess the cell performance. Reporting the curves of the photoanode and the photocathode on the same graph, as represented in figure 1.3 , it is then possible to identify working point of the tandem cell. The working point corresponds to the intersection between the two electrical characteristics, where current and potential are equal (J_{op},V_{op}). In solar fuels, efficiency is directly proportional to J_{op}.
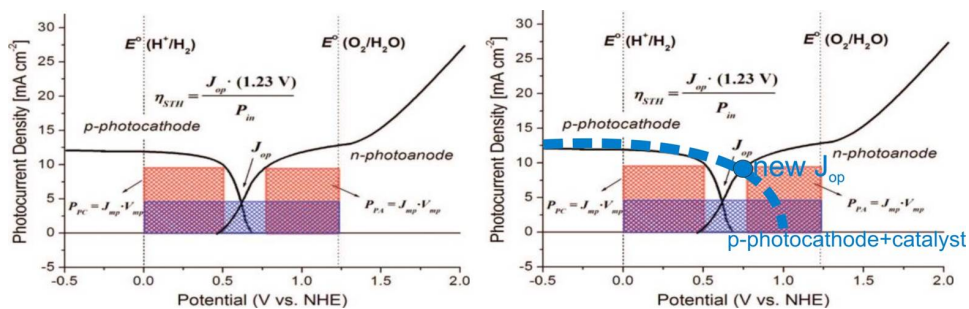
Figure 1.3: electrical characteristic of a tandem device. With catalyst application on the photocathode a shift of the the curve toward higher potential values is expected (represented with the dashed blue line). Figure used with author autorization [36]
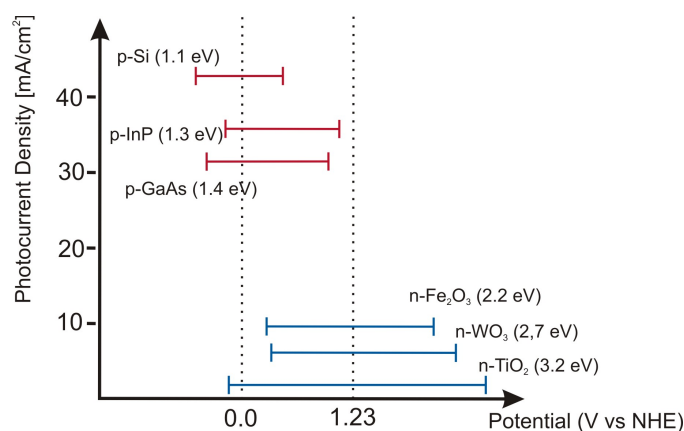
Figure 1.4: Examples of p- and n-doped semiconductors (respectively reported in red and blue) with correct band edge positions to be applied in PEC tandem devices. As reported in the graph, generally the chosen material for the photocathode has a smaller band gap than the one for the photoanode, whilst able to generate larger photocurrent density.

Thus, the highest performance for a tandem PEC device is obtained when the J_{op} point is as close as possible to the individual maximum photocurrent of the two photoelectrodes [36]. Once the semiconductor photoelectrodes are chosen,the working point can be modified by reducing overpotentials by means of an electrocatalyst. In this regard, several semiconductors have appropriate band edge positions for the PEC water reduction/oxidation (see figure 1.4), but the kinetic aspects of HER/OER on the bare semiconductor surface generally limit the yield of the reaction. To decrease these overpotentials (i.e. increase the kinetics of the reaction), a catalyst must be interfaced with the semiconductor surface. In the case of a photocathode interfaced with the catalyst, the illuminated I/V curve will shift towards higher potentials. As a consequence, the tandem device efficiency will increase (see blue curve in figure 3).

This project focuses on the study of transition metal calchogenide MoS_2 as electrocatalyst on Silicon and its development as efficient photocathode. The reasons of this material selection will be explained in the section *materials choice*. In the next section I will describe in details the catalyst role in HER.

1.2   The catalyst role in hydrogen evolution reaction

The addition of a proper catalyst on the photocathode surface has a critical effect on the overall PEC device performance by decreasing the kinetic overpotential of the hydrogen evolution reaction.

To have an effective increase of the HER, the catalyst must have a good electrical connection with the semiconductor underneath. The main reason
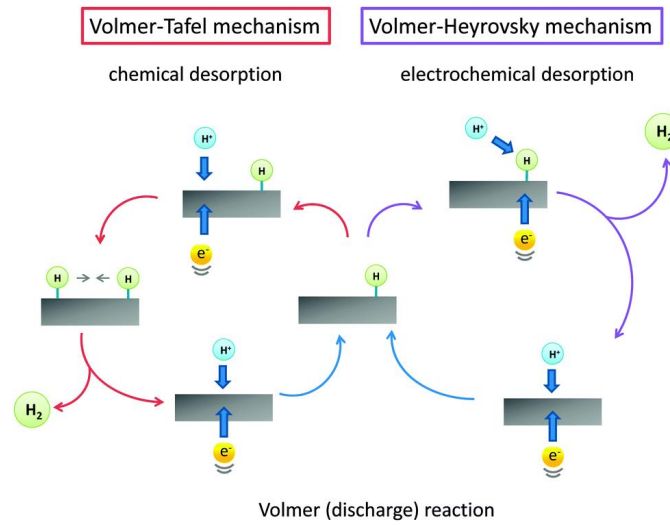
Figure 1.5: Schematic representations of the different steps involved in HER reaction. Figure used with author authorization [28]

is that the catalyst works as a preferential site for photogenerated minority carrier injection (which are electrons in this case). Secondly, it must have a catalytically active surface for HER, in order to effectively increase the kinetics of reaction. Finally, an effective catalyst must be robust enough to maintain its efficiency over time scales relevant to commercial use.

It has been proven that 3 steps are involved in the conversion of $2H^+$ to H_2, commonly referred as the *Volmer*, *Heyrovsky* and *Tafel* steps:

$$Volmer: \quad H^+ + e^- \rightarrow H_{ads} \tag{1.3}$$
$$Heyrovsky: \quad H_{ads} + H^+ + e^- \rightarrow H_2 \tag{1.4}$$
$$Tafel: \quad H_{ads} + H_{ads} \rightarrow H_2 \tag{1.5}$$
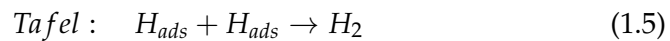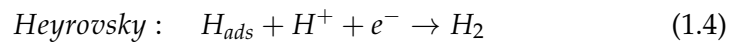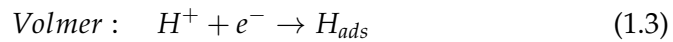
Step 1 precedes in any case, instead a not completely understood combinations of steps 1-2 or 1-3 lead to the final production of H_2, being the two reactions close in Gibbs activation energies [32, 12]. In the first step, photogenerated electrons, which are driven to the interface, combine with protons in the vicinity to form hydrogen atoms, that adsorb at the surface. After that, two of these adsorbed atoms can combine together generating hydrogen molecule (Tafel step). Alternatively one adsorbed H atom can react with an H^+ that is reduced by another photogenerated electron driven at the interface (Heyrovsky step). Once the hydrogen molecule is formed, it leaves from the site of the photocathode. A schematic representation is given in Fig. 1.5.

It is important to underline that both the adsorption and desorption steps require an activation energy. In this regard, the catalyst is effectively
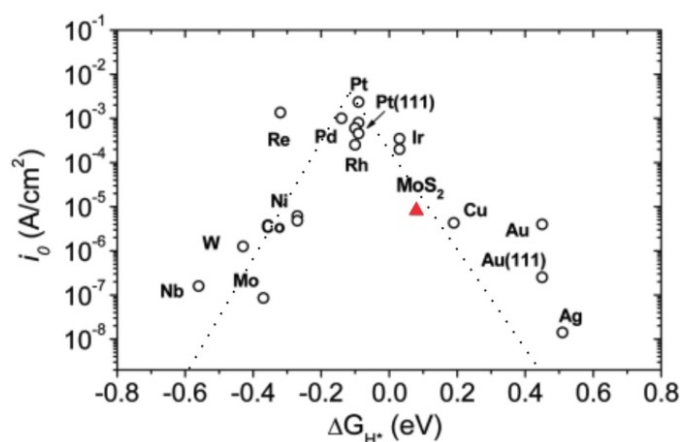
Figure 1.6: Volcano plot for MoS_2 and pure metals with the exchange current density as function of the DFT-calculated Gibbs free energies of H atom adsorption. Figure used with author authorization [32]

active for HER when the activation energy is low, consequently increasing the kinetics of adsorption and desorption.

A common representation used to classify HER catalyst is the so called "Volcano" relation. This one is obtained plotting the measured values of exchange current density versus the hydrogen Gibbs free adsorption energy. The Volcano plot shows that the catalytical activity has a maximum at intermediate values of bond strength between the H atom and the catalyst surface (see figure 1.6) .

Until now the platinum is the unbeatable catalyst for HER with an exchange current density of $4.510^{-4} A/cm^2$. Many experimental works have shown that platinum high catalytical activity arises from negligible hydrogen adsorption activation energy at its surface [10]. This metal is usually deposited on the semiconductor surface as nanoparticles.

However, platinum is extremely expensive and not suitable for a large scale application, therefore scientists have been trying to explore other cheap and Earth abundant materials to substitute it. Norskov and co-workers predicted the HER activity of many materials by using the density functional theory (DFT). This theoretical analysis, supported by many experimental works, have found in MoS_2 a suitable candidate, able to compete with platinum (see figure 1.7) [22].

A detailed report on the recent experimental proofs of MoS_2 HER activity is given in the next section.
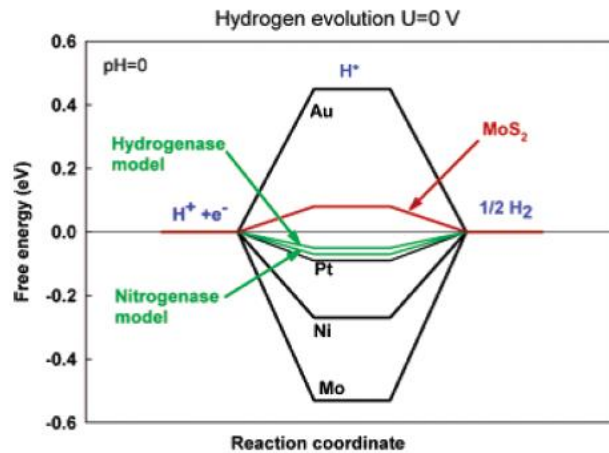
Figure 1.7: Calculated free energy diagram for HER at a potential $U = 0$ vs SHE and $pH = 0$. The Gibbs free energy of H atoms adsorption on the different catalyst surfaces is found computing the difference in free energy respect to molecular hydrogen. The included result for MoS_2 required to increase the H coverage from 25 to 50% in the calculations. Figure used with the authors authorization [22] .

1.3 Materials choice

As presented in the previous sections a photochatode for tandem PEC cell is composed by two main components: the semiconductor absorber material and the catalyst. To date, the most efficient photochatode based on a p-type semiconductor has been achieved using p-InP with a dispersion of Pt nanoparticles on top, yielding a conversion efficiency of 13.3% [15]. However both these materials are scarce and not suitable for large scale production.

Indeed in this project *Silicon* and MoS_2 were selected with the goal of using Earth abundant and relatively cheap materials as photocathode.

P-type silicon (Si), with a resistivity between 0.1 and $0.5\Omega cm$, has been chosen as semiconductor material for the photocathode. This specific doping level was selected in accordance with a previous work done in "Laboratory of semiconductor materials" (LMSC, EPFL) [40]. Silicon has a band gap of $1.1eV$ and conduction band edge that straddles the hydrogen evolution standard potential. Moreover, it is relatively stable in acidic environment and it has been shown that Silicon can be effectively combined with metallic catalysts [13] .

For this project two different chrystallographic orientation of the Silicon substrate were used: <111> and <100>. This was done to observe any changes in the catalyst growth due to the substrate orientation. Moreover, hexagonally ordered micro- and nano-pillars Si arrays were used. These

(a) *Three dimensional representation of MoS$_2$ structure.*

(b) *Structure of 2H polytype of MoS$_2$.*
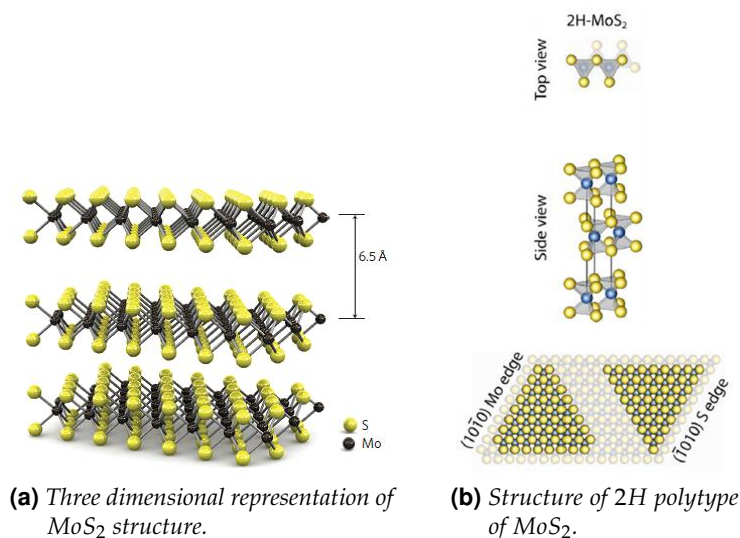
Figure 1.8: Scematic representation of MoS_2 compound.Figure used with the authors authorization [30] .

substrates were fabricated by a combination of optical lithography and deep reactive ion etching [16].

On the other hand, molybdenum disulphide (MoS_2) has been selected as Earth abundant catalyst to be applied on p-type Si surface. MoS_2 belongs to the layered transition-metal chalcogenide family of materials. MoS_2 crystals are composed of vertically stacked weakly interacting layers, held together by van der Waals forces as shown in Fig. 1.8.

This material has the peculiar property to switch from an indirect band gap of $1.2eV$ in the bulk form to a direct band gap of $1.8eV$ when in monolayer form. Moreover, it has an outstanding stability in acidic environment, which is fundamental to be combined in a tandem cell. In recent years, MoS_2 has been identified as the perfect candidate to substitute Pt, both by theoretical calculations and by experimental works. The computational results obtained using DFT showed not only that MoS_2 should be highly active for HER, but also that only the edges are interesting in this context and the basal plane is catalytically inactive. In fact, the activity arises from the sulphur atoms, 2-fold coordinated to the metal atoms, exposed at the edges,which are able to bind hydrogen with a low activation energy of the order of $0.1V$ [22].

Shortly after this theoretical prediction, the good activity of MoS_2 was confirmed experimentally by MoS_2 nanoparticulates. In agreement with the computational results, these experiments found a high catalytic activity of the uncoordinated sulphur atoms at the $\bar{1}010$ edge. This is due to the metallic character of these atoms, that allow for a more effective adsorption

of H^+ [23] . However, the per-site activity, also called "turnover frequency", of MoS_2 edges was still $50 - 100$ times lower than Pt one. For that reason, after having identified the nature and position of the active sites in this compound, the race was on in improving the HER performance of the material. The two general approaches were to increase the nominal activity of each site or to improve the number of active sites.

In the former case three different ways have been shown to be promising [6] :

- to activate the S-edges by doping ;

- to modify the H adsorption energy by tuning the interactions of the catalyst with the substrate;

- to tune the electronic properties through Li ions intercalation and to use the conductive 1T polymorph of MoS_2 ;

Regarding the increase of active sites in MoS_2, the idea is to nanostructure the catalyst, so that the number of accessible edge sites per geometric area increases. With this end, nanowires, nanoparticles and modified thin films have been explored.

Furthermore, in the nanostructure design, it is very important to keep into account the conductivity between the active sites and the semiconductor underneath: electrons and holes mobility is about 2200 times faster in MoS_2 along a basal plane than between the layers. For these reasons a potentially good MoS_2 nanostructure design should show a high amount active sites exposed to the electrolyte contact, having these sites connected to the semiconductor by the basal planes. In such design the sheets made of basal planes stuck parallel each others with vertical aligned respect the substrate as shown in figure 1.9.

To achieve these goals, several works presented the development of different core shell structures obtained by the sulfurization of previous patterned MoO_3 which lead to achieve a generally good activity [24, 9] . MoS_2 basal planes vertically aligned to the substrate have extremely high geometrical area of the catalyst and a good electrical connection to the substrate [37] . Secondly, this alignment could guarantee a limited light reflection by the catalyst, avoiding a reduced photon absorption in the semiconductor underneath.

However, even if outstanding activities have been presented in different works using nanostructured MoS_2, the synthesis of the catalyst was always performed on standard conductive substrate, such as gold or black carbon and only in a second step transferred on the selected absorber [25]. This transfer does not allow to exploit the potential advantage of a vertical allignment respect to the substrate.
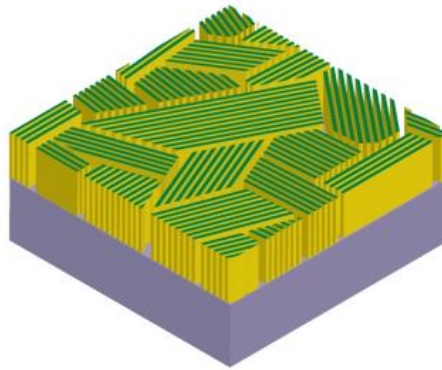
Figure 1.9: Schematic representation of vertically aligned MoS_2 sheets. Figure used with the authors authorization [7] .

1.4   Motivations and objectives of the project

Both p-type Si and nanostructured MoS_2 have been separately proved to be suitable for efficient cost-effective components in PEC tandem cells [36]. The aim of this project is to directly interface MoS_2 nanostructures with Silicon , by using a relative cheap and industrially scalable technique:atmospheric pressure chemical vapour deposition (AP-CVD). The objectives are to asses the growth of nanostructured MoS_2 on p-type Si substrates and to modulate the exposure to electrolyte of active edges. Photocathodes have been developed and characterized to asses the sunlight driven HER performance.

Summarizing, the project is divided into two main parts:

- A first part focuses on the study and modulation of the growth of MoS_2-based nanostructures, directly grown on different p-type silicon by AP-CVD;

- A second part focuses on the development and characterisation of a lab-scale photocathode by means of photoelectrochemistry.

Chapter 2

Experimental techniques

2.1 Atmospheric pressure chemical vapour deposition

Atmospheric pressure CVD is used in this project since many works proved that this technique is suitable for the synthesis of nanostructured MoS_2 [39] . AP-CVD involves the chemical reaction of the selected gaseous reactants on or in proximity to the heated substrate surface where the product of the chemical reaction is deposited. This technique is versatile and industrially scalable, being able to provide highly pure materials with a good structural control.

The AP-CVD system used in this project is composed by a four zone furnace equipped with a $32mm$ outer diameter quartz tube, which is directly connected to the gas sources (H_2, H_2S and Ar) at one edge, and to the exhaust line to the other . A thermocouple is set in the middle of the furnace as temperature gauge during the deposition process. The furnace temperature and the gases flow is directly controlled by a LabVIEW software. To deposit MoS_2 nanostructures the chosen precursors are gaseous H_2S and solid MoO_3 powder (99.9998% Alfa Aesar™). Moreover ultrahigh purity Argon and H_2 are used as transport and reducer gases, respectively. A schematic representation of the described set-up is reported in figure 2.1.
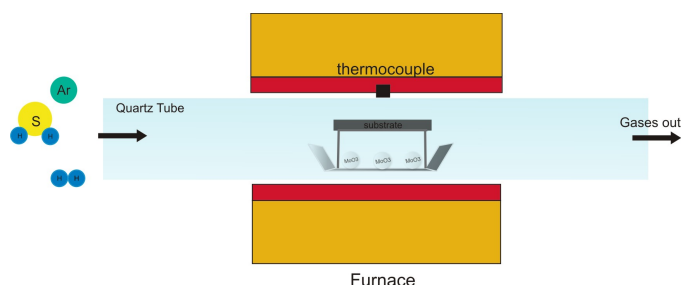
Figure 2.1: Schematic representation of the CVD apparatus used for the catalyst deposition.

Figure 2.2: Picture of the CVD set-up used for the catalyst growth.

A first step of cleavage of the selected substrate in squares of $12mm^2$ is performed, followed by the consecutive sonication in acetone, $2-propanol$, DI-water and a final etch in buffered HF (Alfa Aesar$^{®}$), in order to remove native SiOx. After being cleaned, two squares are fixed on a stage made with a Mo bent wire and placed face-down above an alumina crucible containing around $5mg$ of MoO_3 powder (experimental error of $1mg$) in 3 spherical balls. These powder balls are always located in the same positions in the crucible, in order to get uniformity between the different growth processes. Two chips of the same dimensions of annealed sapphire are placed in the same way at the borders of the stage. These chips are used as references, since the growth of MoS_2 on sapphire by CVD has already been studied [14] . Moreover, due to their optical transparency, it is easier to assess the presence of deposited material with a fast analysis in the optical microscope. The crucible is then loaded into the furnace and placed at its centre in proximity to the thermocouple. All the four zones of the furnace are maintained at the same temperature during the process. In figure 2.2 is reported a picture of the used apparatus.

After the preparation of the experimental set-up, a desired recipe is selected setting a value for all the changeable parameters reported in figure 2.3.

The temperature setting, gases flow and $Ar/H_2S/H_2$ ratio define the main variables in our recipe, always keeping a general process line: a first step of tube flushing with $200sccm$ of Ar for $10min$ at a temperature of $300°C$. Then Ar flow is decreased down to $10sccm$ followed by a ramp to the selected temperature ($T_{entrance}$) with a rate of $50°C/min$. Once $T_{entrance}$ is reached, H_2S and H_2 valves open and the temperature is further increased
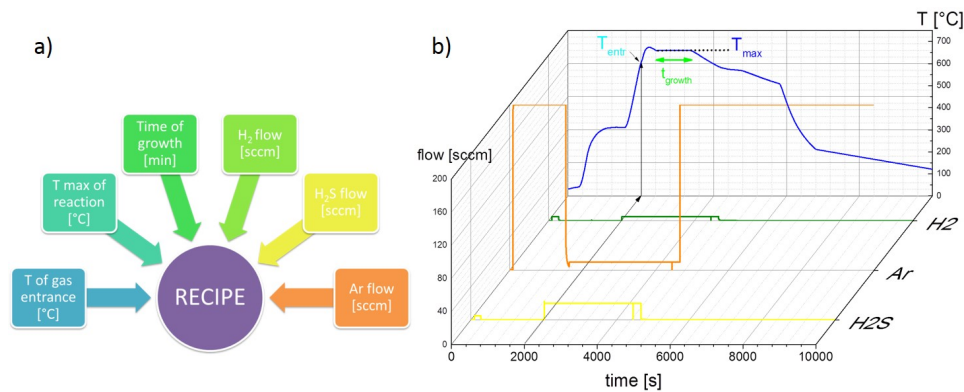
Figure 2.3: a)Diagram of the different parameters involved in the selection of a deposition recipe. The temperature of entrance is the temperature value reached in the chamber at which the gaseous precursors are introduced. The maximum temperature of reaction is the maximum value of temperature reached in the chamber during the deposition and the time of growth is the time passed at this temperature.b)Variation of the selected parameters during the deposition process.

up to T_{max}. T_{max} is maintained for t_{growth} (normally $10min$). After the growth, the furnace is cooled down to $570°C$ and H_2S and H_2 flows are stopped. During the cooling down Ar flows at $200sccm$. All the variation in temperature and gas flows are recorded in real time during the deposition process. An example of a growth process is reported in figure 2.3.

For some samples, as it will be exposed in *Growth study and modulation* from chapter 3, a further step of sulfurization is performed in the same apparatus.

For sulfurization, the as-grown sample is fixed on the *Mo* stage and placed face-up to the empty alumina crucible. After that it is loaded in the middle of the furnace.

The process line is as follows: a first step of tube flushing with $200sccm$ of Ar for $10min$ setting the temperature at $300°C$. Then the Ar flow is decreased down to $10sccm$ in parallel with the entrance of $5sccm$ of H_2 and $20sccm$ of H_2S . Then temperature is increased up to $700°C$, and is maintained for $30min$. After sulfurization the furnace is cooled down to $500°C$ at which point H_2S and H_2 flows are stopped. At the same time Ar flow is increased up to $200sccm$ and the furnace is left to cool down to room temperature.

2.2 Raman and Photoluminescence spectroscopy

Raman spectroscopy

Raman spectroscopy is a widespread non-destructive technique based on the detection of optical phonons by inelastic light scattering, which can be used to study the vibrational properties of crystals. In this project, Raman spectroscopy is used to assess the presence of MoS_2 crystal grown by AP-CVD and to obtain a qualitative measure of its thickness. The analysis is focused on the detection of the two most intense Raman active modes of $2H - MoS_2$: the E_{2g}^1 and the A_{1g}^1 located respectively at $380cm^{-1}$ and $405cm^{-1}$. The former is related to in plane vibrations of the atoms, while the latter refers to the out of plane vibrations. It has been shown that for exfoliated MoS_2 layers the relative difference in frequency between the two modes is thickness dependent. By increasing MoS_2 thickness, the E_{2g}^1 mode red shifts and the A_{1g}^1 a blue shifts [26] . Therefore, it is possible to use Raman frequencies as a qualitative indicator of the analyzed MoS_2 thickness (see figure 2.4).
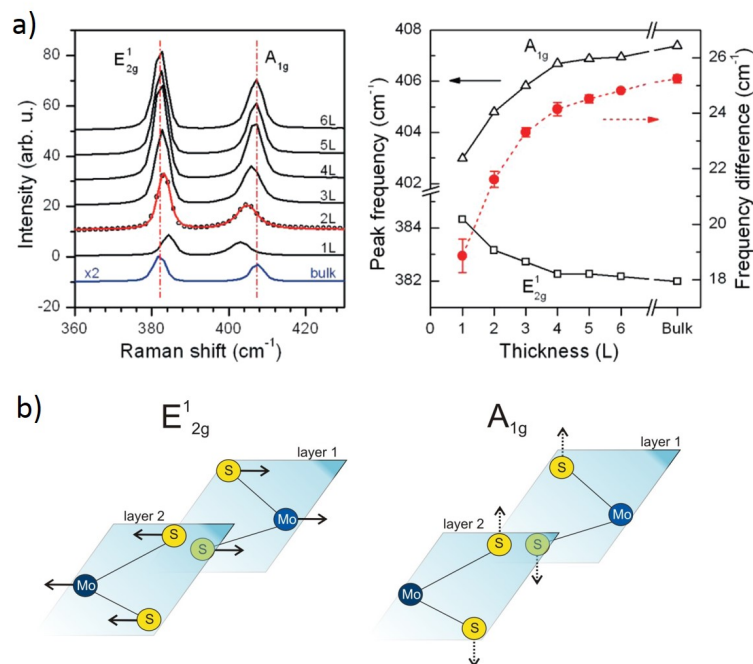
Figure 2.4: a)Reported variation of the mode frequency gap in function of the number of analyzed layers for exfoliated MoS2 sample.Figure used with the authors authorization [26] . b) Schematic representations of the two vibrational modes analyzed.

Unpolarized Raman scattering measurements are carried out at room

temperature in the back-scattering configuration using a laser ($Ar - Kr$) with wavelength of $488nm$ and power of $1mW$. The scattered light is collected and then analyzed with a triple spectrometer (Princeton trivista, $SP2500i$) equipped with a liquid nitrogen-cooled charged coupled device (CCD). All the presented spectra are obtained by the sum of 5 separate spectra with an acquisition time of $30s$. A first set of measurements is performed on samples grown with the same set-up on annealed sapphire substrates as reference spectra. In these spectra are present the two typical peaks related to MoS_2 at $\sim 380cm^{-1}$ and $405cm^{-1}$. Moreover a decrease in the frequency gap is observed as the thickness of the analyzed MoS_2 decreased. The gap values for the single MoS_2 triangle are in accord with the values found in literature related to the MoS_2 monolayer modes.
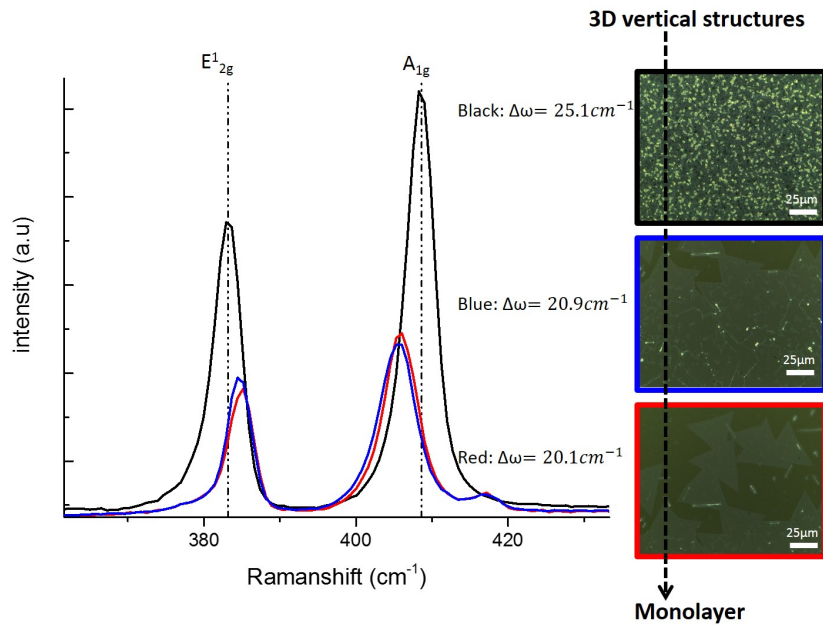
Figure 2.5: Raman spectra obtained by samples grown on annealed sapphire substrates by AP-CVD. The reported optical images show different achieved morphologies, from $3D$ vertical structures down to monolayer one.

Photoluminescence spectroscopy (PL)

PL spectroscopy is a non-destructive technique extremely useful to characterize the electronic states of the analyzed material. In this project, PL is used to get information on MoS_2 band structure and to qualitatively asses its thickness. MoS_2 has a transition from indirect to direct band gap moving from bulk material to monolayer [33] . Due to this behaviour a much stronger emission (around $659nm$) [14] is expected for monolayer MoS_2
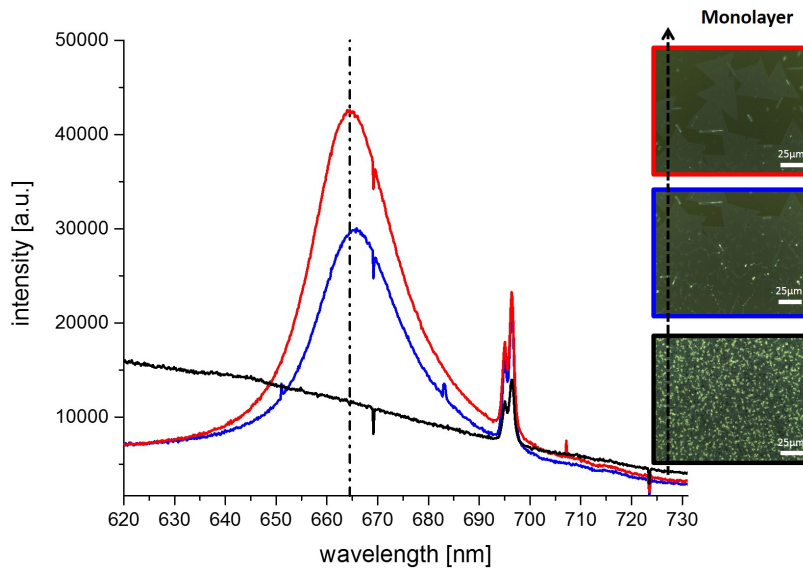
Figure 2.6: PL signals for sample grown on annealed sapphire substrates. The peak at $667nm$ is referred to MoS_2, the two at $695nm$ are due to the sapphire impurities.

with respect to the bulk MoS_2.

PL measurements were performed at room temperature, using an input $Ar - Kr$ laser with wavelength of $488nm$ and power $200\mu W$. The emitted light is analyzed with a single grating spectrometer (Andor $SR - 5001 - D1 - R$) equipped with a thermoelectrically cooled CCD. All the presented spectra result from an acquisition time of $1min$, subtracting the background.

Also for this technique, a first set of measurements is done on samples grown on annealed sapphire as reference . The comparison between emission from different MoS_2 structures is reported in figure 2.6.

A strong emission peak at $667nm$ is observed only for samples with flat horizontal triangles. This indicate the monolayer nature of these structures, as opposed to vertical ones.

2.3 High resolution X-ray diffraction (HRXRD)

In this project, a *high resolution x-ray diffractometer* (Empyrean, PANalytical) is used to get structural and compositional information of the grown structures. The samples are characterized with the Gonio scan configuration presented in figure 8. High intensity $Cu \ K\alpha_1$ radiation line ($\lambda = 0.15406nm$) is used and is kept at a fixed incident angle with respect to the sample. The detected angle range from 10° to 65° in order to cut off the main Si peak at 70°. The sample spins during the measurement to analyze all the different in-plane
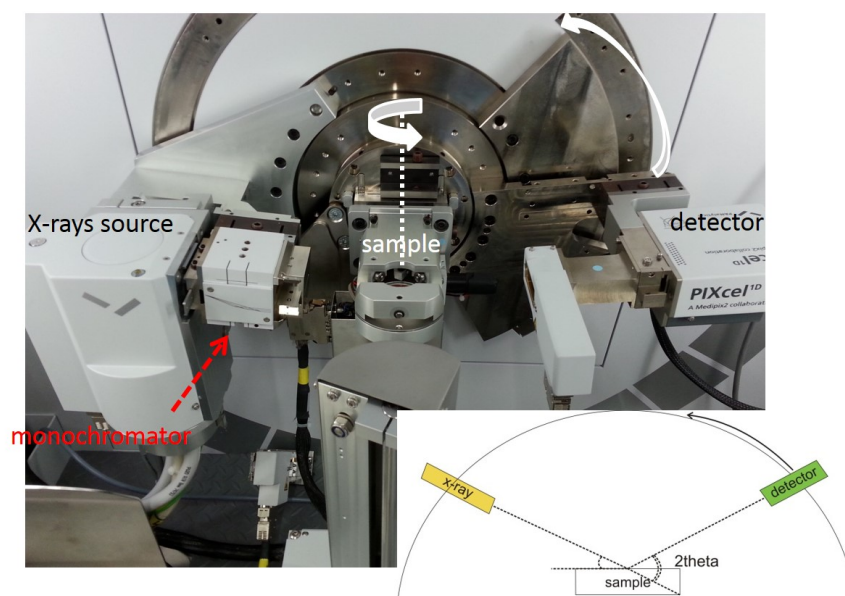
Figure 2.7: Picture of the used set up. In the right corner is reported a schematic representation of the Gonio configuration.

crystallographic orientations. Moreover a knife made of lead is placed next to the samples to cut off the scattering noise and improve peaks sharpness.

2.4 Scanning electron microscopy (SEM) and atomic force microscopy (AFM)

2.4.1 SEM

In this project, SEM imaging of the samples has a fundamental role to easily assess the different morphologies of the grown catalyst. Due to the different conductivities of the substrate surfaces used in this project, scanning electron microscopes (SEM $Leo1550$ and SEM Jeol $JSM - 6701F$) are used changing the voltage from 3 to $10kV$, maintaining the standard aperture of $30\mu m$. For some samples also cross section images are shown, in order to give a better visual impact of the grown structure profile.

2.4.2 AFM

AFM (Bruker FastScan) correlated with silicon tip on nitride lever (Bruker SCANASYST-AIR-HR) is used to measure the profile of the sample surface after catalyst growth. The measurements are done oscillating the cantilever at a frequency of $130kHz$ and scanning a surface of $1mm^2$. To assess the average profile of a sample 5 different zones are scanned. Unfortunately,

due to the vertical morphology the analysis often requires long scanning time and the utilization of many tips. For these reasons, only few samples are characterized with this technique.

2.5 Photoelectrochemical characterisation

In this project, an analysis of the total electrode activity is performed in order to asses any improvement in the Si based photocathode by MoS_2.

To prepare a lab-scale photocathode, the backside of the AP-CVD grown samples is scratched, wetted with Ga-In eutectic (Aldrich-chemistry, $495425 - 5G$) and finally contacted to a copper wire fixed on a microscope slide with conductive Ag paint (Ted Pella®). All the electrical connections are carefully sealed in a glass pipette or covered with epoxy (Araldite®), in order to avoid any contact with the liquid electrolyte.
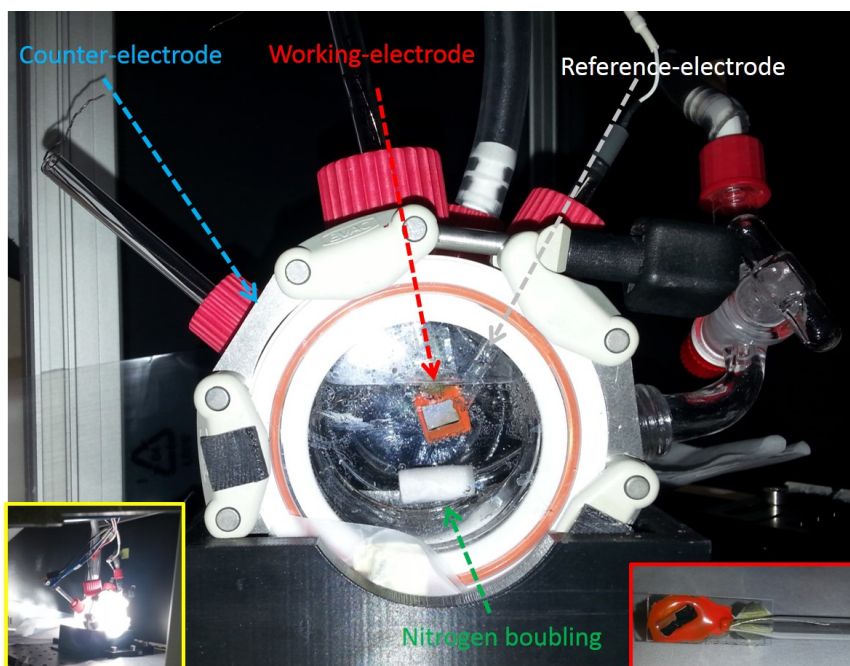
Figure 2.8: Picture of the photoelectrochemical cell used during the tests. In the bottom left corner it is reported a picture of the cell under illumination, and on the bottom right is a picture of the prepared lab-scale photocathode.

The photoelectrode is tested in a glass photoelectrochemical cell, reported in figure 2.8. This cell has a 3 electrodes configuration: the reference electrode ($Ag/AgCl$, Basi $MF - 2052RE5B$), the non-photo active counter electrode (made with a Pt wire) and the working electrode (lab-scale photocathode). All the 3 electrodes are dunk in a H_2SO_4 based electrolyte with pH

0 and connected to a potentiostat (Bio Logic,$SP - 300$) . A solar simulator (Sciencetech A4 Solarlight line) equipped with a $230W$ Xenon arc lamp is used as light source. An optical fiber focuses the light beam perpendicularly to the photocathode surface. During the test, high purity N_2 gas is bubbled in the liquid electrolyte to move the electrolytic solution. To test the photocathode, current/voltage cycles are performed both in dark and under 1 Sun of illumination. A potential range between 0 and $-1.5V$ is scanned at a rate of $100mV/s$ for 10 times both in dark and in light conditions. The test is always completed with a single curve of linear sweep voltammetry extended in the same potential range and performed with a scanning rate of $20mV/s$ under chopped light conditions. Finally, all the obtained curves are normalized dividing the obtained photocurrent values for the exposed surface area of the sample.

After the tests, the I/V curves obtained under illumination are analyzed and compared. To analyze a sample I/V curve, we have to understand at which voltage the photocurrent starts. This voltage value is determinate by the overpotential involved in the reaction.

In this project, we have arbitrary decided to take as overpotential the voltage value at which the current density reaches $-5mA/cm^2$. We expect an overpotential reduction with the catalyst application.

Bare Silicon samples are also prepared and tested, in order to have reference curves.

Chapter 3

Results and discussions

This chapter is divided into two main sections, in line with what stated in the section *Motivation and objective of the project* from chapter 1.

I start by reporting on the results concerning the study and modulation of the MoS_2 nanostructure growth on p-type Silicon by atmospheric pressure CVD. This study is completed showing growth results on the different types of p-type Si substrate used: planar <100> and <111> oriented Si, micro- and nanopillar Si arrays.

Moreover during the project, functionalization with thin coatings of planar p-type <100> Si surface has been done for two reasons:

- Because Si oxidizes during the AP-CVD process (as it will be described in details in the next section *Characterisation of designed lab-scale photocathodes*)

- To study the catalyst growth and interface on other surfaces

In the second section, I report the results regarding the electrochemical characterization of lab-scale photocathodes made with the AP-CVD grown samples.

3.1 Growth study and modulation

During this Master project, more than 50 growth processes have been performed. The growth procedure is described in detail in section *Atmospheric pressure chemical vapour deposition* from chapter 2. $T_{entrance}$, T_{max}, H_2S flow, H_2 flow and $time_{growth}$ were systematically tuned. Only one parameter a time was changed in order to understand its role in the catalyst growth. A table with all the tried recipes is reported in *Appendix B*. In all cases, growth of nanostructured MoS_2 was observed.

Moreover, a non uniform covering of the substrate area was always obtained as can be assessed by the picture of the substrate chip after the
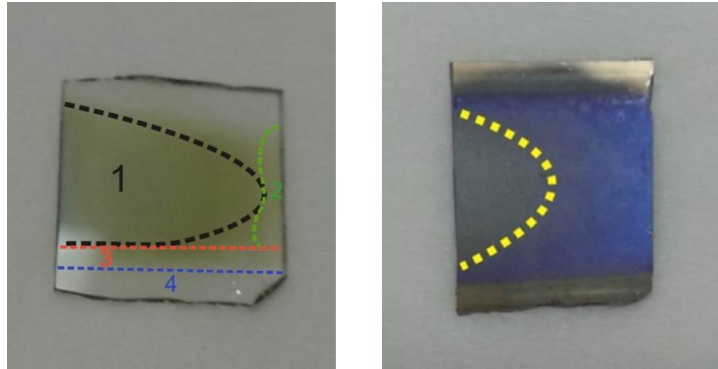
Figure 3.1: Picture of the substrate chips both sapphire and Si after the deposition process. The uncovered stripes are the areas in contact with the Mo stage during the process.

process (figure 3.1). We suspect that the non uniformity of the deposit amount, is due to the concentration of the molybdenum precursor in 3 spherical particles which leads to a non uniform access of its vapour during the deposition. On the other hand, the gaseous sulphur precursor flows homogeneously on all the surface, being this precursor directly introduced in the gas phase. As a consequence, a different stoichiometric ratio of the reactants is suspected across the chip.

Since the growth is not uniform on the whole substrate area, in all the comparisons reported in this work only the region of the chip with the highest material density is considered.

After evaluating the grown samples, it is found that MoS_2 morphology is clearly modified by changing the deposition parameters.

The parameters that give highest impact on morphology are:

- the maximum temperature reached during the deposition process (T_{max})

- The entrance temperature of the gaseous precursors H_2S and H_2 ($T_{entrance}$)

By increasing the *maximum temperature*, the morphology is finely tuned from $2D$ planar nanostructures to $2D$ vertical nanoflakes, as shown in the figure 3.2.
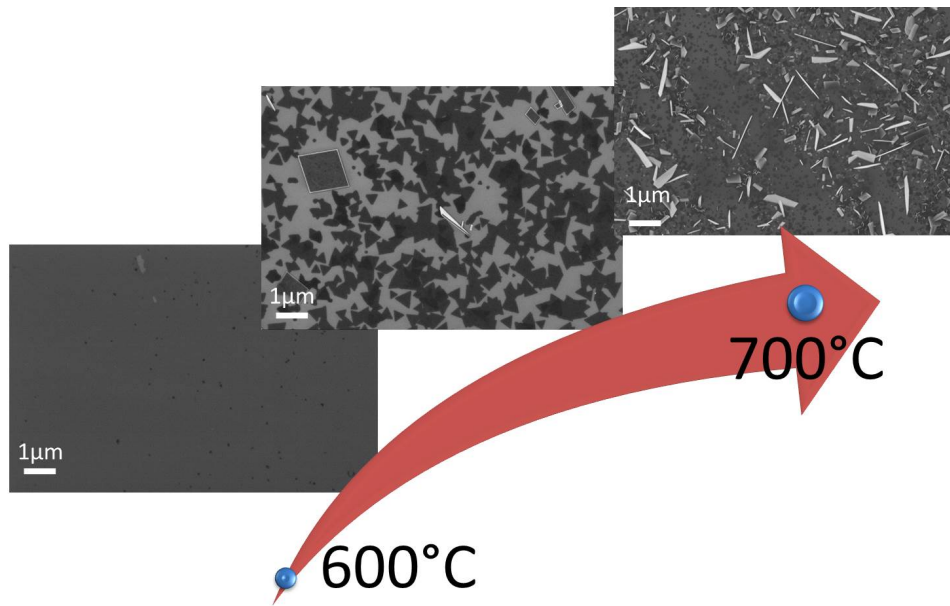
Figure 3.2: Collection of SEM images of samples grown at different maximum temperature values. From the left to the right the T_{max} value are 600, 665 and 700°C. $time_{growth}$ is set at $10min$. The gas flows and ratio are kept fixed. The Si substrate has a <100> crystallographic orientation.

We believe that the different morphologies arise from a different growth mechanism.

While the growth of planar MoS_2 nanotriangles originates from the reaction of MoO_3 and H_2S both in gas phase, growth of vertical flakes consists on a 2 step process. $2D$ structures obtained are similar to the ones reported in other similar works.

In the latter, the maximum temperature in the chamber is high and this increases the amount of MoO_3 vapour. Due to the larger availability of oxide, MoO_3 nanoflakes start to grow on Si substrate. At this point, the oxide nanoflakes serve as source and template for the MoS_2 growth. In fact, the incoming H_2S flow sulfurizes the surface of the *pre-grown* structure, leading to the possible formation of a core-shell structure. Being the sulfurization process in parallel to the oxide growth, the flake size width is limited.

On the other hand, if the *gas entrance temperature* is increased, the length and the density of the nanoflakes is also increased. A comparison of the samples grown at different entrance temperature is reported in figure 3.3.
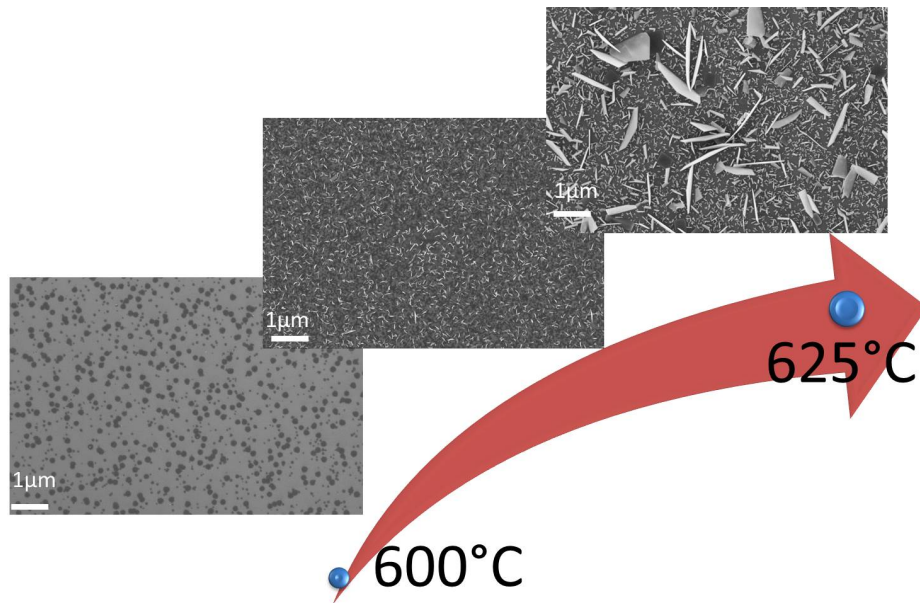
Figure 3.3: Collection of SEM images of samples grown at different entrance temperature values. From the left to the right the $T_{entrance}$ value are 600, 615 and 625°C. T_{max} is fixed at 700°C. $time_{growth}$ is set at 10*min*. The gas flows and ratio are kept fixed. The Si substrate has a <100> crystallographic orientation.

Changing $T_{entrance}$ by 25°C, it is possible to increase the average flakes length from 200*nm* up to 2*μm*. This result is a further confirmation to the previous stated hypothesis. In fact, the time at which H_2S is introduced is directly linked to $T_{entrance}$. The higher the temperature, the longer is the substrate only exposed to the oxide vapour. This means that for higher $T_{entrance}$, there is more time for the oxide nanoflakes to grow before being sulfurized, increasing their density and length.

A comparison between the reference Raman and PL spectra as a function of morphology are reported in figure 3.4. These analyses were done following the procedures described in *Raman and Potoluminescence specroscopy* from chapter 2.

The reported Raman spectra show that MoS_2 is present in all the different kind of samples, since the two typical vibrational modes at $\sim$ 385 and $405cm^{-1}$ are present.

Moreover, it is possible to observe that samples with only 2*D* planar structures show a smaller gap between the vibrational mode frequencies in comparison to the vertical nanoflakes. Comparing this reduced frequency gap with the values found in literature and with the ones measured for samples grown on sapphire substrate (both reported in *Raman spectroscopy* from chapter 2), we conclude that the thickness for planar 2*D* MoS_2 structures is
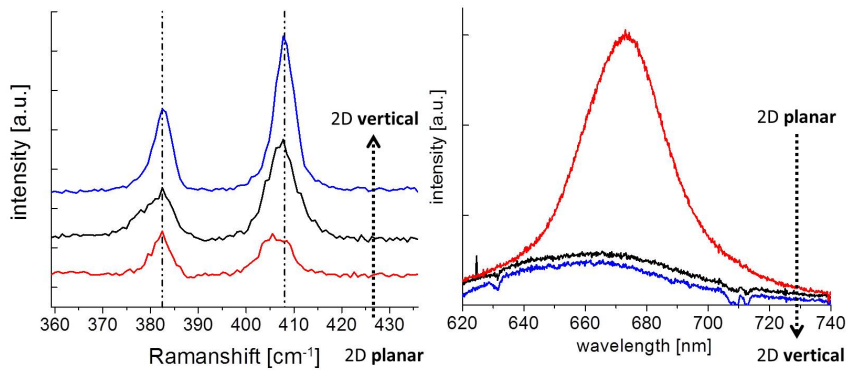
Figure 3.4: Comparison of Raman (on the left) and Pl (on the right) outputs for samples which show a different morpology.

only of a few layers.

The thinner nature of 2D MoS_2 planar structures with respect to vertical nanoflakes was confirmed also by photoluminescence. Figure 3.4 shows a strong enhancement of the band-to-band emission from 2D planar structures, which indicates direct nature of its band gap.

Furthermore, I report a comparison between different XRD spectra as a function of the growth morphology. The analysis was performed following the procedure reported in *High resolution x-ray diffraction(HRXRD)* from chapter 2.
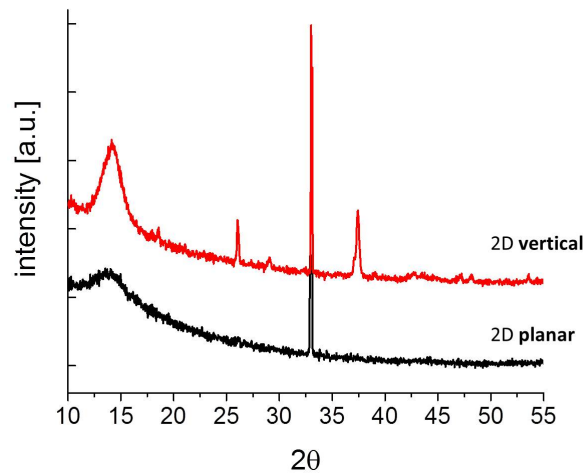
Figure 3.5: XRD output of a sample with 2D planar structures compared with the one with nanoflakes.

In both the reported XRD spectra it is possible to notice the presence of a peak at 14,2° referred to 2H MoS_2 hexagonal phase with crystallographic direction [002]. The reference card is reported in *Appendix B*.

The other peaks appearing in the sample with nanoflakes correspond to MoO_2 monoclinic phase. The two most intense ones at 26° and 37° are attributed to directions [011] and [020] respectively. The high intensity and sharpness of the oxide peaks indicate a very good crystallinity and a large grain size.

The absence of the MoO_2 peaks in the sample with only $2D$ planar structures is in agreement with the two growth mechanisms described above. In fact, the lower growth temperature used for $2D$ horizontal structures offers a limited MoO_3 vapour during growth. As a result, a complete reaction of the evaporated molybdenum precursor with sulphur occurs before reaching the substrate.

On the other hand, the presence of both MoS_2 and MoO_2 peaks for the samples with nanoflakes reinforce our hypothesis to have a first step of growth of oxide nanoflakes followed by sulfurization. However, since MoO_2 peaks are observed, it is clear that not all the oxide is sulfurized.

A qualitative characterization of the surface of as-grown samples is done with AFM, following the procedure described in *Atomic force microscopy (AFM)* from chapter 2.

$3D$ maps for $2D$ planar and nanoflake morphologies , are compared in the figure 3.6.
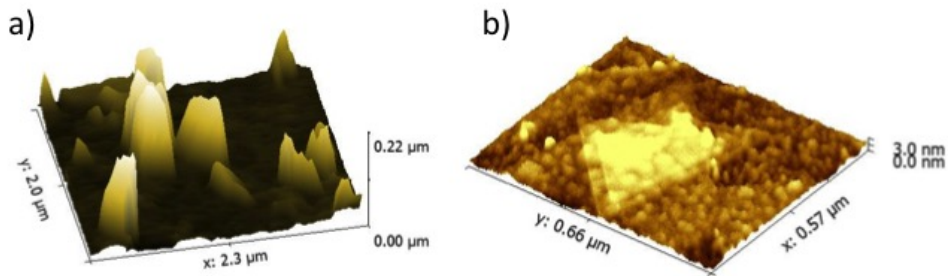
Figure 3.6: Profile $3D$ maps of samples with nanoflakes (on the left) and $2D$ planar (on the right)morphology respectively. a) Samples grown at $T_{max} = 700°C$, $T_{entrance} = 605°C$. b)Samples grown at $T_{max} = 665°C$, $T_{entrance} = 605°C$; image courtesy of Eleonora Frau,LMSC,EPFL. All the other parameters are kept constants and the substrate is planar p-type Si with <100> as crystallographic direction

The height of vertically aligned nanoflakes can be up to $1\mu m$. On the planar case, MoS_2 grows in a triangular shape, with the tendency to form a thin film. It is important to consider that the only difference between the two cases is the amount of MoO_3 vapour promoted by the different temperature.

We suspect that also in case of vertical nanoflakes , a thin planar MoS_2 film of is formed between the vertical structures. Unfortunately, the com-

plexity of this morphology and the high nanoflakes density prevents AFM analysis focused in these regions.

During this project, also H_2 and H_2S flows and ratio were tuned. The rule to change only one parameters at a time was always kept, in order to understand the effect produced changing the flow of each gas and the role of the overall gas amount in the tube. To see all tried combinations, please refer to the reported table in *appendix B*.

No clear changes in the growth morphology were observed from this systematic tuning.

Raman, PL and XRD analyses show no appreciable difference either.

This result is unexpected, since by increasing H_2S amount in the tube, we expect to obtain planar morphology, inducing a complete reaction of the MoO_3 vapour.

From this observation, we can assume that the amount of oxide vapour is too high at $T_{max} \geq 700°C$ to completely react in the gas phase even if the sulphur flow is set at a value close to allowed limit for the used set-up.

Since the vertical alignment is observed for all the gas conditions we assume the latter does not determine morphology. Therefore, vertical structure can be considered as preferential morphology of growth of the oxide on Si substrate at $T_{max} \geq 700°C$ and $T_{entarnce} \geq 605°C$.

After that, a change in time spent at the highest temperature (t_{growth}) was performed. Also in this case, no variation in the growth morphology were observed changing this parameter.

This result suggests that the growth of oxide nanoflakes is fast and subsequently stopped by reaction with sulphur. This could be the reason why a strong increase in the length and density of nanoflakes is not observed, even when t_{growth} is increased by a factor of 10, as reported in the figure 3.7.
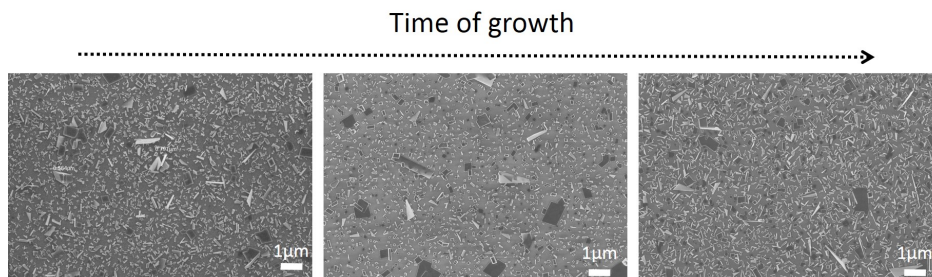
Time of growth

Figure 3.7: Collection of SEM images of samples grown at different time of growth values. From the left to the right the t_{growth} is 2,10 and 20 min respectively. T_{max} is fixed at 700°C and $T_{entrance}$ at 605°C. The gas flows and ratio are kept constant.

As already reported, the vertical geometry of MoS_2 catalyst is desired so that a larger number of active sites are in direct contact with the electrolyte. At the same time, the catalyst-semiconductor contact may be improved due to the larger electron mobility along the basal planes of MoS_2 structures.

In this regard, to better understand this promising nanoflakes morphology, further experiments have been done on these samples.

In order to better understand how MoS_2 shell is formed an additional sulfurization step was performed. The procedure followed for this step, is described in details in section *Atmospheric pressure chemical vapour deposition* from chapter 2.

SEM imaging before and after the sulfurization step does not show any change in the nanoflakes morphology: the vertical alignment with respect to the substrate is kept (see figure 3.8).
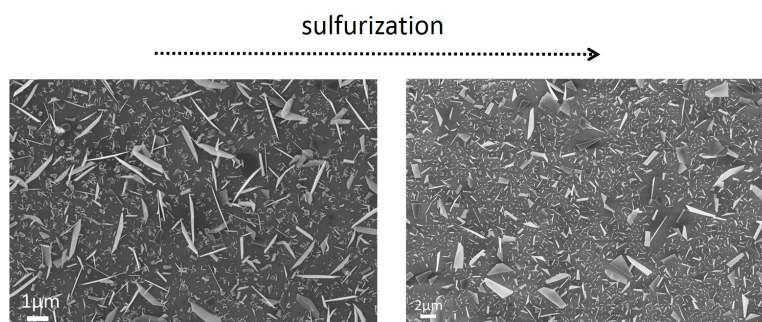
sulfurization

Figure 3.8: Collection of SEM images of the same sample before and after the sulfurization step. Sample grown on planar p-type Si at T_{max}=700°C,$T_{entrance}$= 605°C, H_2S flow of 15$sccm$ and H_2 flow of 5$sccm$.

A comparison between the XRD outputs before and after sulfurization is reported in the figure 3.9.

From the comparison between the XRD outputs before and after sulfurization step, it is possible to observe:

- A drop in the MoO_2 peaks intensity after the sulfurization step

- A dramatic increase of the intensity and sharpness of the MoS_2 peak at 14°

- The rise of a second characteristic MoS_2 peak at 44° referred to 2H MoS_2 with crystallographic direction [006]

These changes indicate an effective decrease of the molybdenum oxide content with an increase of MoS_2. Moreover, the increase in sharpness of the first MoS_2 peak and the appearance of a second one, reveal an increase in the grain size and crystal quality.
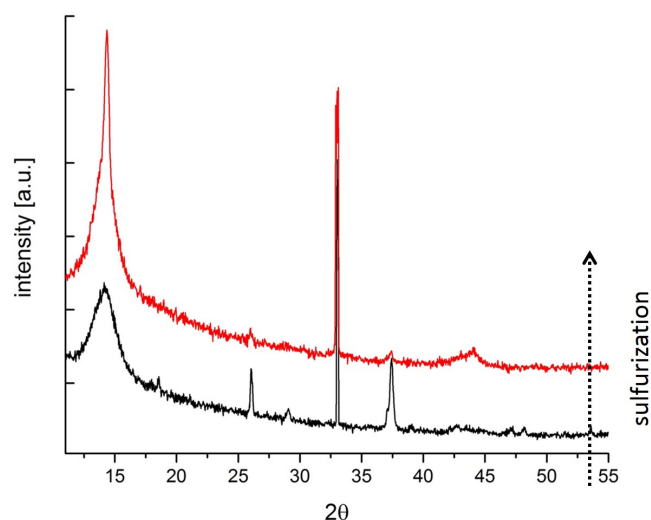
Figure 3.9: Comparison between XRD output of the same sample before (black spectrum) and after (red spectrum) the sulfurization step.

These observations, seem to confirm that MoS_2 growth by sulfurization of Mo in the pre-grown MoO_2 structures.

To better understand MoS_2 formation and structure, *scanning transmission electron microscopy (STEM)* and *electron energy loss spectroscopy (EELS)* were performed by Prof. Jordi Arbiol's group from *ICN*2 in Barcelona.

Both annular dark-field imaging (ADF) method and EELS were performed simultaneously to map the nanoflake surface and to obtain chemical composition, respectively. The analyses performed on nanoflakes *as grown* (i.e. before the sulfurization step) are reported in the figure 3.10.

To map the chemical elements, M-edges for molybdenum, K-edges for oxygen and L edges for sulphur were used.

As seen in the maps, Mo is distributed homogeneously throughout the whole nanoflake. S signal related to MoS_2 is clearly located inhomogeneously at the edge of the nanoflakes structure, whereas O signal related to MoO_2 is observed in the inner part of the nanoflakes .
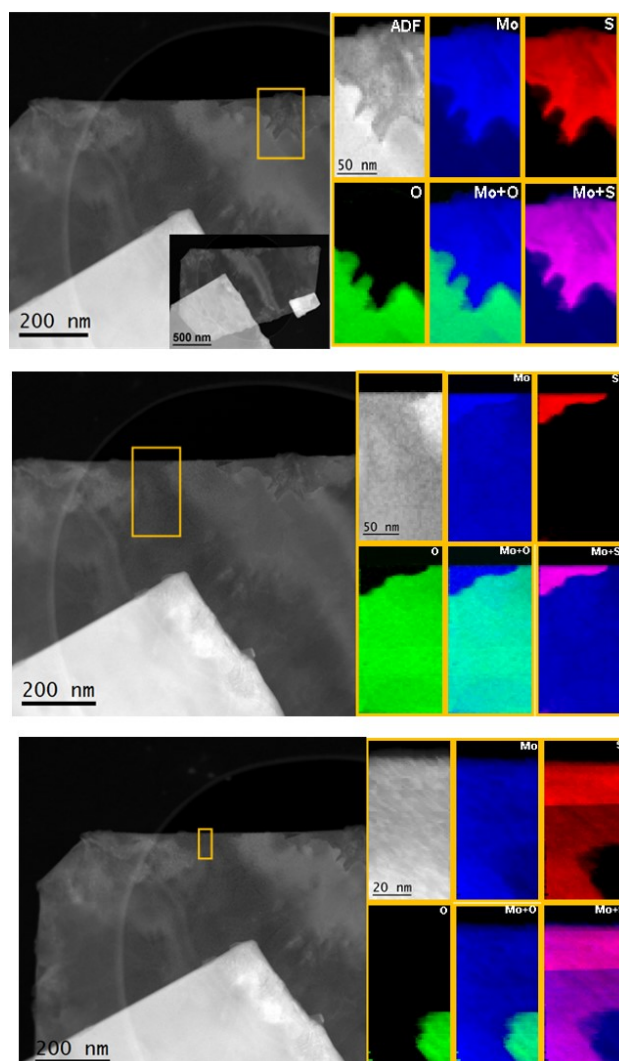
Figure 3.10: Collection of EELS chemical composition maps referred to yellow rectangled area of the STEM-ADF micrograph of nanoflakes before the sulfurization. Individual Mo (blue), S (red) and O (green) maps and their composite. The inset included in the first picture corresponds to a low magnification image of the whole nanoflake. Images courtesy of Prof. Arbiol's group.

Using *High resolution transmission electron microscopy (HRTEM)* they confirmed the inhomogenous distribution of MoS_2 on the surface with varying thicknesses. Images of the analysis are reported in figure 3.11.
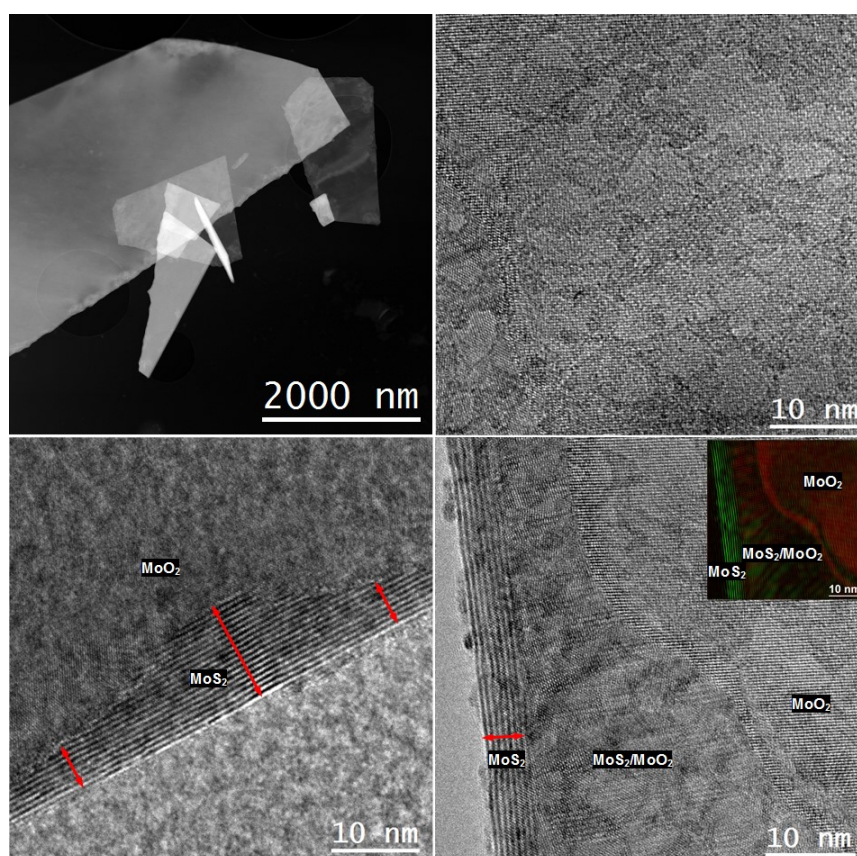
Figure 3.11: ADF STEM general view (top left) and HRTEM micrographs corresponding to different nanoflakes. Images courtesy of Prof. Arbiol's group.

Similar analyses were performed on sulfurized samples. The obtained maps are reported in the figure   3.12.

Figure   3.12 shows the chemical composition of three different flakes.

In the first image, *Mo* and *S* are homogeneously distributed throughout the whole probed region. *O* signal is almost absent, indicating full sulfurization of *as grown* structure.

Meanwhile, full sulfurization is not reached for all nanoflakes, as shown in the other two reported images.

Moreover, the images show that the rough part at the edges can be related to the sulfurization regimes and the smooth part can be retaining MoO_2 species.
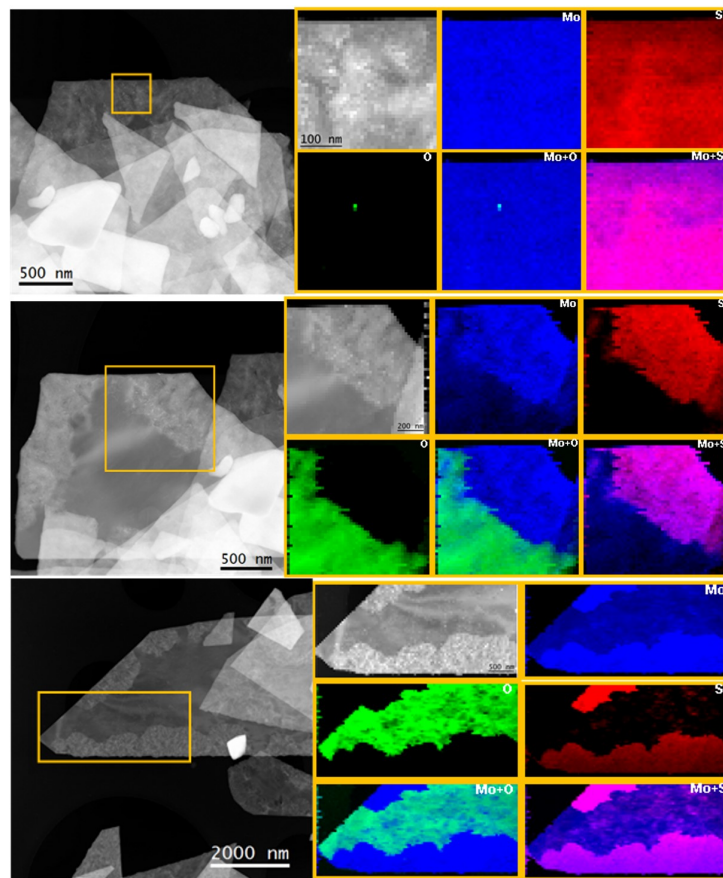
Figure 3.12: Collection of EELS chemical composition maps referred to yellow rectangled area of the STEM-ADF micrograph of nanoflakes after the sulfurization. Individual Mo (blue), S (red) and O (green) maps and their composite. Images courtesy of Prof. Arbiol's group.

From these analyses it can be concluded that:

- Sulphur concentrates only at the lateral edges of the nanoflakes and it is almost absent on the two main surfaces

- sulfurization is a gradual process from the outermost to the inner part of the nanoflakes

The higher MoS_2 covering of the nanoflake surface after the sulfurization step is attested by HRTEM images which are reported in figure 3.13.
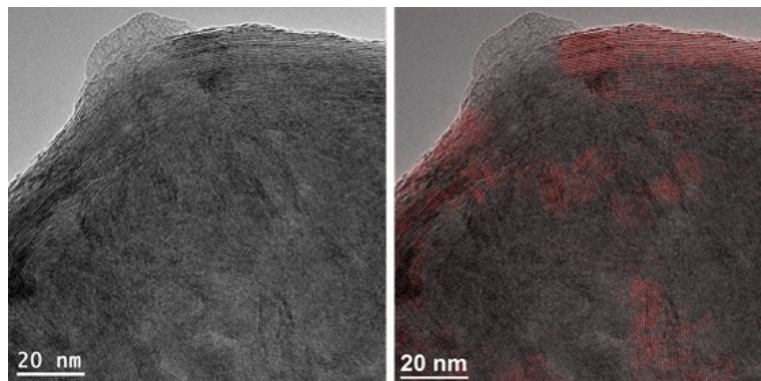
Figure 3.13: HRTEM images showing the surface of a typical nanoflake after the extra sulfurization process. On the right [002] planes of the Molybdenite 2H phase are marked in red. Images courtesy of Prof. Arbiol's group, Advanced electron nanoscopy, ICREA.

Therefore, it seems that the edges are preferential sites for the sulfurization reaction and that a complete core-shell heterostructure is normally not achieved even after the sulfurization step. Further cross-section analysis are planned to confirm this hyphotesis.

Furthermore, since only one recipe of sulfurization was tried, it could be interesting to tune the process parameters to observe if a complete sulfurization of all nanoflakes can be reached.

In order to observe any difference in the catalyst morphology induced by the substrate crystallographic orientation the growth was performed simultaneously on on planar p-type Si with two different orientations: <100> and <111>.

However, no evident change in the morphology of the deposited material was observed, as reported in figure 3.14.

<100> <111>
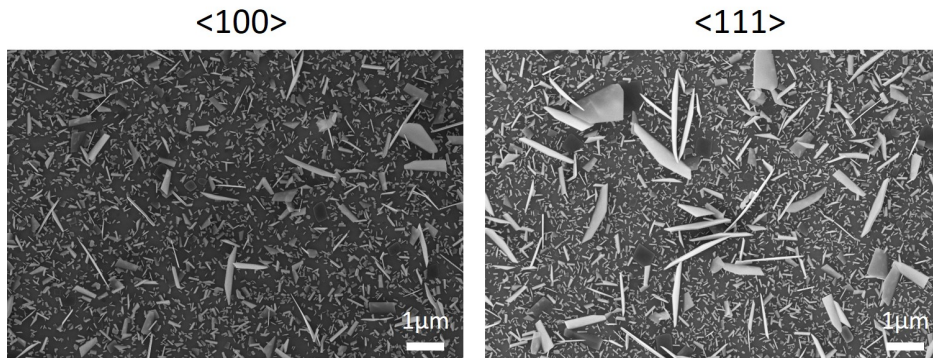
Figure 3.14: SEM images of the same growth performed on two Si chips with different crystallographic orientation .

Therefore, we can assume that growth morphology is not governed by Si substrate crystal orientation but by growth parameters (i.e. ratio of the incoming precursors).

This is different to the growth on sapphire substrate, where the nanoflakes growth is oriented in function on the substrate orientation.
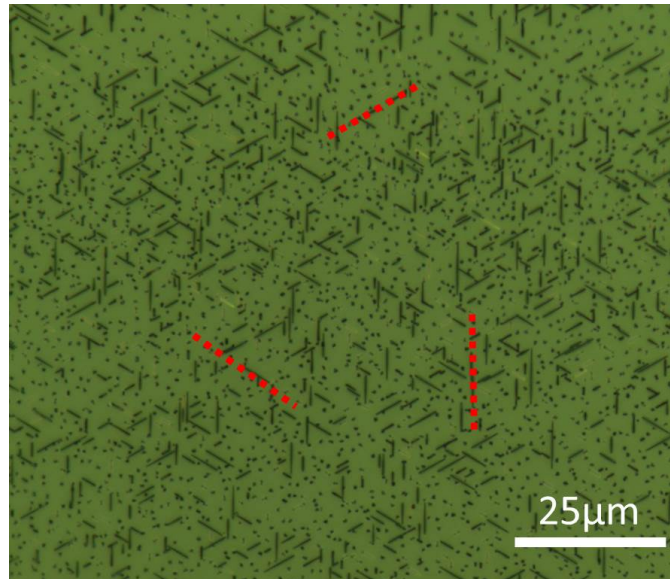
Figure 3.15: Optical image of nanoflakes grown on annealed sapphire. The observed preferential growth orientation are marked with red dot lines.

The shown insensibility of nanoflake growth direction in function of the Si substrate orientation is indication of the decoupling of crystal properties with the substrate and seems to orient just perpendicularly to the substrate

During the project, different p-type Si substrate morphologies were used

moving from planar to micro- and nano-pillars array structures.

Figure 3.16 shows SEM images of samples grown under under same parameters but on different substrate morphologies.

Interestingly, nanoflakes perpendicular to all the surfaces are found regardless to Si morphology. The use of micro and nano pillars is of high interest for solar fuel applications. The reason is twofold. On one hand, these structures have anti-reflection properties that allow improved light harvesting. On the other hand, the larger surface area allows a larger catalyst loading.
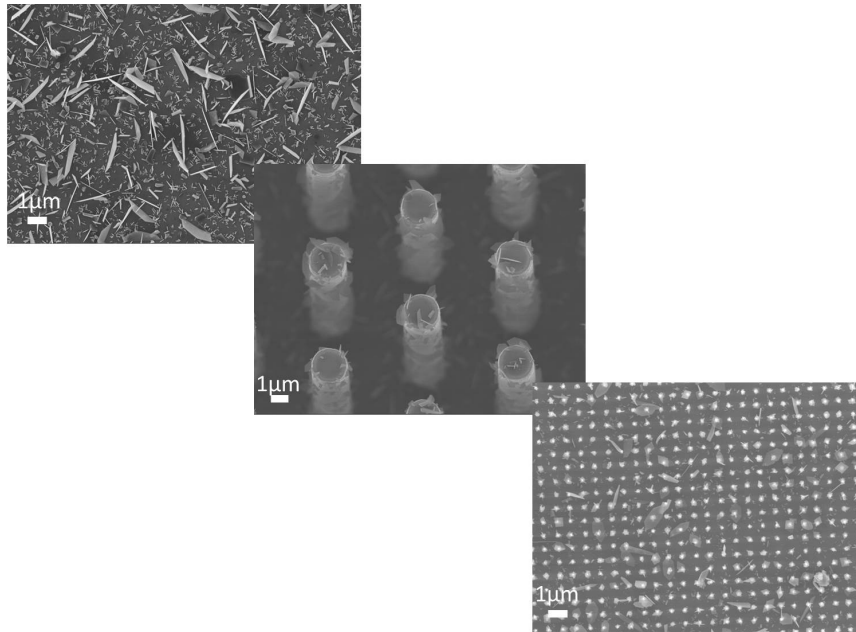
Figure 3.16: Growth performed on planar Si, micro-pillar array and nano-pillar array. Deposition parameters: $T_{max} = 700°C$, $T_{entrance} = 605°C$, $t_{growth} = 10min$, $H_2S = 20sccm$, $H_2 = 5sccm$. Si crystallographic orientation is <100>.

We observed that using AP-CVD technique, catalyst growth is not limited to the top facet of the Si pillars, but it is spread overall the exposed Silicon surface as shown in figure 3.17.

Side view   *Top view*
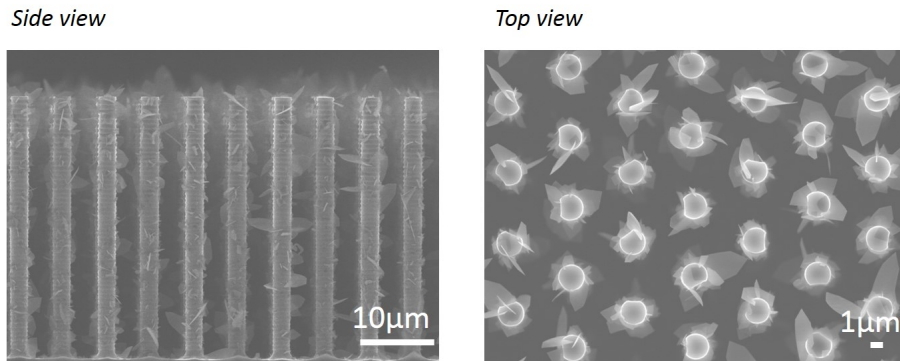
Figure 3.17: SEM images of catlyst growth on Si micro-pillar array. Deposition parameters: $T_{max} = 710°C$, $T_{entrance} = 605°C$, $t_{growth} = 10min$, $H_2S = 15sccm$, $H_2 = 5sccm$. Si crystallographic orientation is <100>.

Similar to planar Si substrates, temperature parameters play a crucial role on the MoS_2 final morphology. By using low growth temperatures, $2D$ thin planar MoS_2 were achieved while at higher temperatures, we obtain nanoflakes structures.

Correspondingly, increasing T_{max} the length of nanoflakes increases.

The length is qualitatively estimated from SEM images and the measured values were plotted as a function of the maximum temperature in figure 3.18.
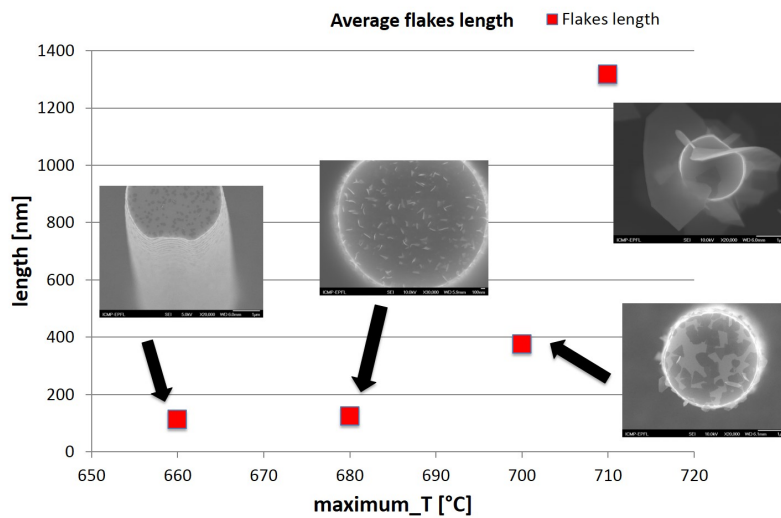
Figure 3.18: Plot of the average flakes length in function of the maximum temperature reached in the chamber during the deposition. Fixed deposition parameters: $T_{entrance} = 605°C$, $t_{growth} = 10min$, $H_2S = 15sccm$, $H_2 = 5sccm$. Si crystallographic orientation is <100>.

By rising the T_{bmax} by 60°C, the flakes length increases from 200nm up to 1.2μm.

Raman,PL and XRD spectra of samples grown under different T_{max} are reported in figure 3.19. The used procedures are described in *Chapter 2*.

We observe no noticeable change in the Raman spectra of samples grown at a maximum temperature of 700°C (blue spectra) and 680°C (black spectra). The frequency difference between the two main modes indicates the presence of MoS_2 with bulk behaviour. The spectrum of sample grown at lowest temperature is not shown because the signal was too weak, due to the lower amount of deposited material.

In contrast, PL shows a strong difference between samples grown at different maximum temperature. We observe a clear band-to-band emission in, samples grown at the lowest temperature (660°C) which indicates the presence of thin structures.

From XRD measurements, we observe a sharp increase of the MoS_2 hexagonal phase peaks at 14° and 44° with increasing T_{max}. Moreover, similar to growths on planar Si substartes, 3 sharp peaks appear related to MoO_2 monoclinic phase in the sample grown at the high temperature ($T_{max} = 700°C$).

In order to reduce the amount of oxide and increase the MoS2 phase a further sulfurization step was performed after growth on some samples with nanoflakes morphology. The used procedure is described in *Atmospheric pressure chemical vapour deposition* from Chapter 2.

No changes in the catalyst morphology were observed due to sulfurization process.

XRD data on a representative sample before and after sulfurisation are reported in figure 3.20.
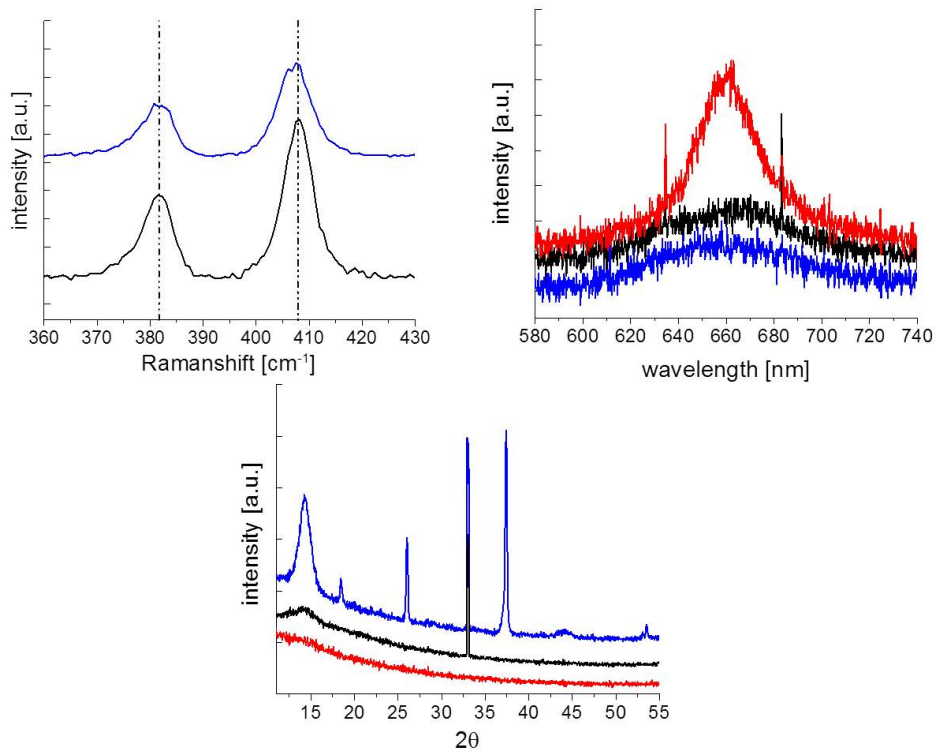
Figure 3.19: Raman (on the right),PL (on the left) and XRD (bottom one) outputs of samples grown at T_{max} of: 700°C for blue spectra, 680°C for black one and 660°C for red one. The other deposition parameters are fixed: $T_{entrance} = 605°C$, $t_{growth} = 10min$, $H_2S = 15sccm$, $H_2 = 5sccm$. Si crystallographic orientation is <100>. Vertical shift are done in all the spectra to make easier the comparison.
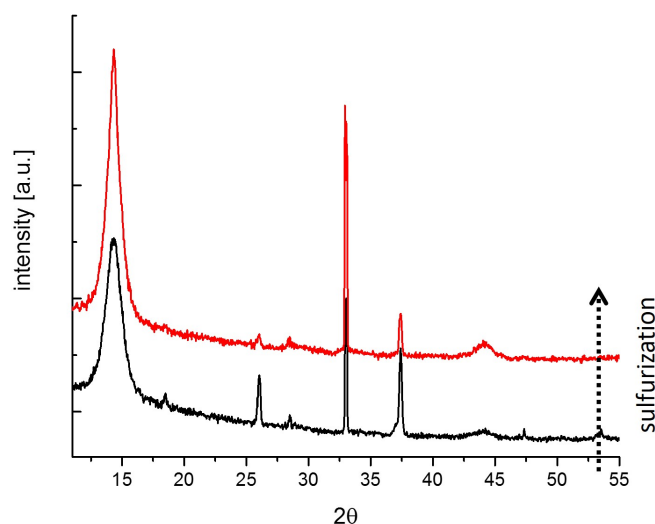
Figure 3.20: XRD outputs of the same sample before (red spectrum) and after (black spectrum) sulfurization step. Deposition parameters are : $T_{max} = 700°C$, $T_{entrance} = 605°C$, $t_{growth} = 10min$, $H_2S = 20sccm$, $H_2 = 5sccm$. Si crystallographic orientation is <100>. Vertical shift are done in all the spectra to make easier the comparison.

In figure 3.20 it can be observed that the sulfurization step induces an increase in the intensity and sharpness of the MoS_2 peaks at 14° and 44° together with a drop in the MoO_2 peaks intensity at 13°,26° and 36°. These changes indicate an increase in the crystallinity and grain size of the MoS_2 deposited structures as in the planar case.

As stated in the introduction of this chapter, the catalyst was grown also on planar <100> Si substrates covered with thin coatings. The chosen coatings are: *titanium (Ti)*, *titania (TiO$_2$)* and *molybdenum (Mo)*.

In this section, I report the results concerning the growth of the catalyst on these functionalized substrates, the role of which will be explained in details in the next section *characterization of designed lab-scale photocathodes*.

Ti coating was applied by using an electron beam evaporator (*Ebeam 2000 evaporator*, ICMP, EPFL), which guarantees a high thickness control and uniformity. Different thicknesses were evaluated . After deposition, a rapid thermal anneal was performed, in order to form the silicide and to increase coating compactness. This step was performed in a rapid thermal annealing furnace (*Annealing 8000C*, ICMP, EPFL). The sample was heated at a temperature of 800°C for 5*s*. The chosen *Ti* thickness are: 1, 2, 4 and 5*nm* all tried with and without the annealing step to observe if it has effectively any influence on the catalyst growth. MoS_2 was grown at same growth conditions in all cases. SEM images of the different samples with and

without post-deposition annealing, are reported figure 3.21. An image of a reference sample grown on bare Si is also shown.
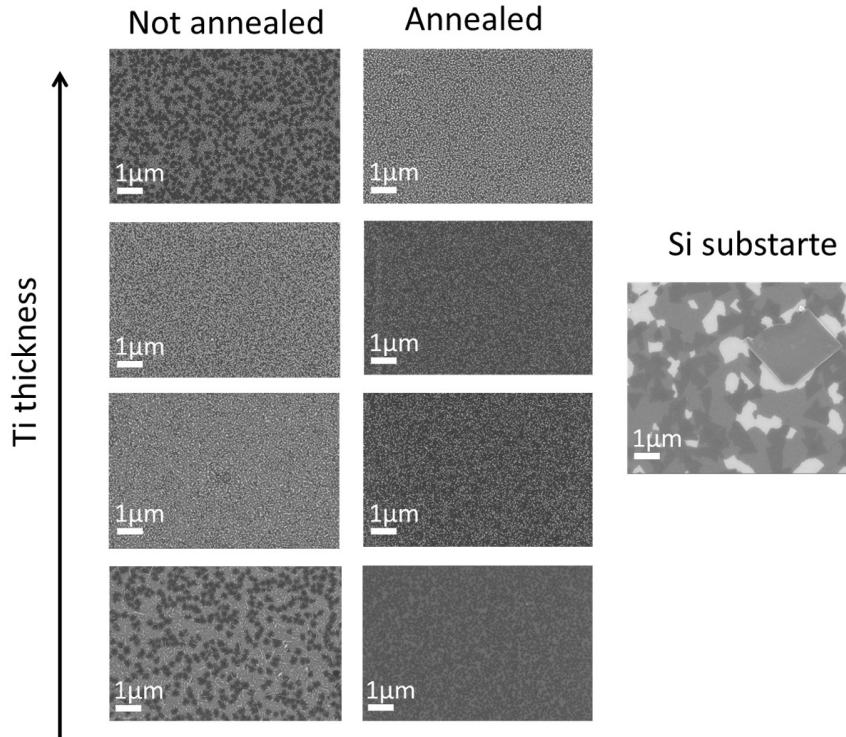
Figure 3.21: Array of SEM images of the samples grown on *Ti* coating annealed and not, compared with a growth on bare Si. Deposition parameters are : $T_{max} = 665°C$, $T_{entrance} = 605°C$, $t_{growth} = 10min$, $H_2S = 5sccm$, $H_2 = 15sccm$. Si crystallographic orientation is <100>.

From the images it is clear the strong impact of the *Ti* layer on MoS_2 growth. Also, the rapid thermal annealing step affects MoS_2 growth.Non annealed substrates show a partial dewetting of the *Ti* coating due to the high temperature exposure during the catalyst growth.

Comparing these images with a growth performed on bare Si, we observe a strong difference in the MoS_2 structures. When *Ti* is present, MoS_2 tends to aggregate in dots (probably alloying with the *Ti* itself), while $2D$ planar MoS_2 grows on planar Si. To confirm the presence of MoS_2, Raman and XRD were performed. Raman spectra of samples with different *Ti* thicknesses and with and without RTA are reported in figure 3.22.

Due to the observation of characteristic MoS_2 Raman peaks, it is clear that MoS_2 is present on all the samples.

Moreover, the intensity of the picks tune accordingly with the amount of material observed in SEM images in figure 3.21. Looking at the SEM images and comparing the mode frequency gap of the different samples, it is
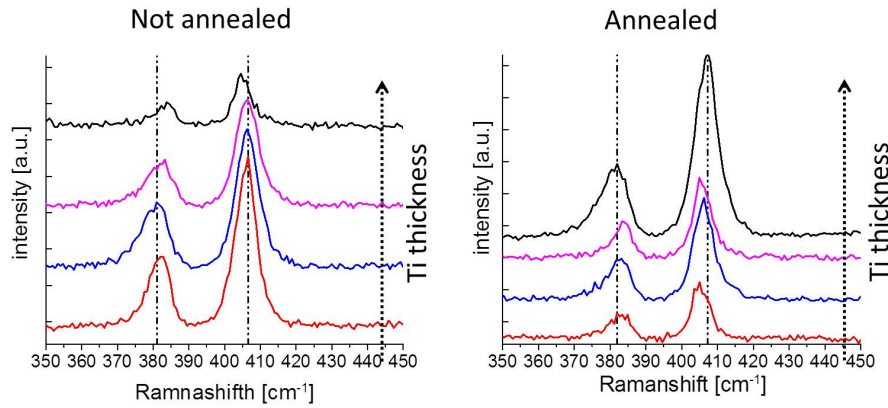
Figure 3.22: Raman spectra reported in function of the thickness of Ti coating annealed and not, Blue spectra refers to $1nm$ of Ti, red ones to $2nm$, black ones to $4nm$ and purple ones to $5nm$.

possible to notice that samples which present $3D$ structures (brighter in the SEM image) have an higher gap respect to samples with planar structures. This is due to the higher thickness of the $3D$ structures with consequent bulky behavior in the Raman output.

XRD data for samples with and without annealing is reported in figure 3.23.
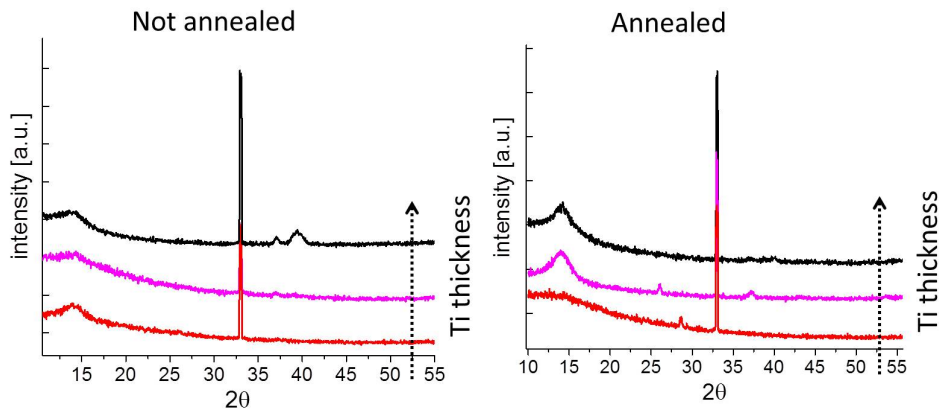
Figure 3.23: XRD spectra reported in function of the thickness of Ti coating annealed and not, Blue spectra refers to $1nm$ of Ti, black ones to $4nm$ and purple ones to $5nm$. The new peaks appearing at 37° and 40° are referred to titanium silicide.

XRD shows that hexagonal MoS_2 grows on $Ti - Si$. From our previous study, we expect a low intensity and broad diffraction peak at 14° for the growth conditions used ($T_{max} = 665°C$ and $T_{entrance} = 605°C$). Growth performed at higher temperatures was also performed ($T_{max} = 700°C$). On

bare Si, higher growth temperatures leads to the growth of vertical MoS_2 nanoflakes.

By contrast, the nanoflakes MoS_2 morphology is not achieved on Si substrate coated with a thin Ti layer even at high temperatures of deposition. (see SEM images in figure 3.24).
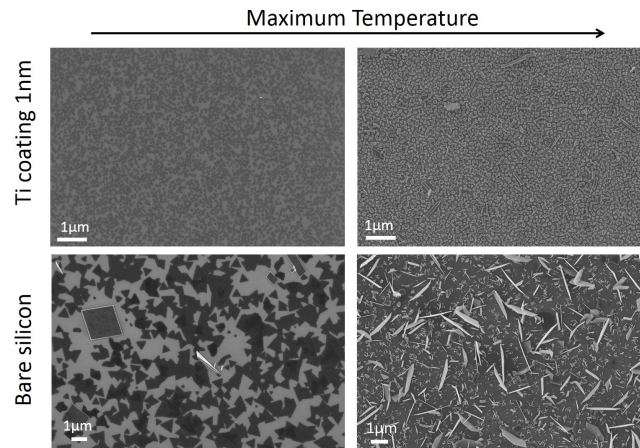
Figure 3.24: Collection of SEM images of samples grown on *Ti* coating of $1nm$ and on bare Si. The T_{max} is increased from 665°C to 700°C. The other parameters are fixed at: $T_{entrance} = 605°C$, $H_2S = 5sccm$, $H_2 = 15sccm$, $t_{growth} = 10min$. Si substrate orientation is <100>.

TiO_2 coating was applied by *atomic layer deposition* (ALD) on the top of the previously etched p-type <100> planar Si substrate. It was used ALD in order to control with absolute precision the coating thickness and obtain a compact layer. The deposition was performed by Eleonora Frau, LMSC, EPFL.

Two different thicknesses were evaluated: 5 and $10nm$. Moreover, a tuning of T_{max} was done to observe if it has any influence on catalyst growth morphology. SEM images of these samples in function of the TiO_2 thickness and T_{max} are reported in figure 3.25 and compared to bare Si.

These samples were characterized with Raman spectroscopy and XRD.

Raman spectra focused on the range of frequencies of interest are reported in figure 3.26 in function of the TiO_2 thickness and T_{max}.

MoS_2 is present in all samples as attested by the observation of the two characteristic modes. Moreover, no sensible changes in the peaks intensity and relative frequency gap are observed both as a function of coating thickness and T_{max}.
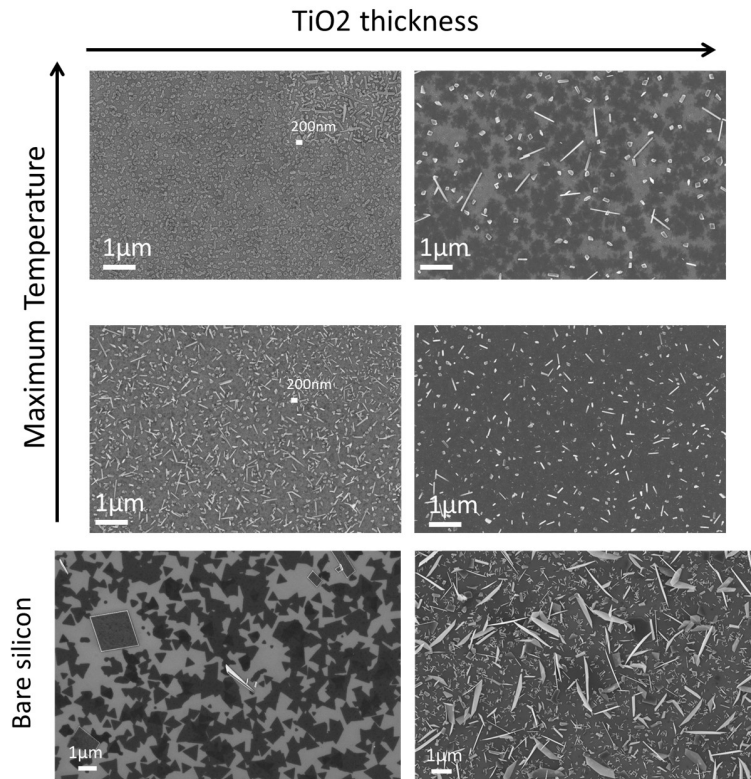
Figure 3.25: Collection of SEM images of samples grown on TiO_2 coating of 5
and $10nm$ and bare Si. The T_{max} is increased from 665°C to 700°C.
The other parameters are fixed at: $T_{entrance} = 605°C$, $H_2S = 5sccm$,
$H_2 = 15sccm$, $t_{growth} = 10min$. Si substrate orientation is <100>.

I report in figure 3.27 XRD spectra of only the samples grown at the
highest temperature, since these have shown the most accentuate features.

From the low intensity and broadness of peak at 14° it is possible to
assume a bad crystallinity of deposited MoS_2 structures. Moreover, it is
possible to notice two peaks associated with MoO_2 at 37° and 56°, which are
expected since the recipe was set at $T_{max} = 700°C$. It is observed also a very
intense peak at 26°, which is related to the presence of highly crystalline
molybdenum titanium oxide (card reported in *appendix B* , reference code
$01 - 072 - 5813$). This observation suggests the reaction of molybdenum
precursor with TiO_2 coating.

Furthermore, it is interesting to notice that no peak referred to TiO_2 is
present. This unexpected result is thought to be a consequence of a too low
annealing temperature set during the ALD process.

Mo coating was applied by e-beam evaporator (*LAB 600H*, CMI, EPFL),
after HF cleaning of the Si substrate. This technique offers a high thickness
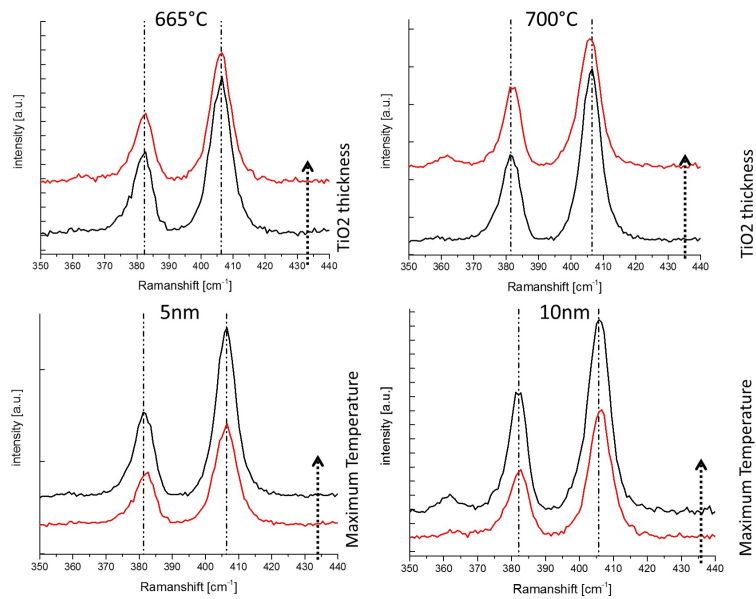
Figure 3.26: Comparisons of Raman spectra in function of TiO_2 coating thickness and selected T_{max}. The T_{max} is increased from 665°C to 700°C. the coating thickness is increased from 5 to 10nm.
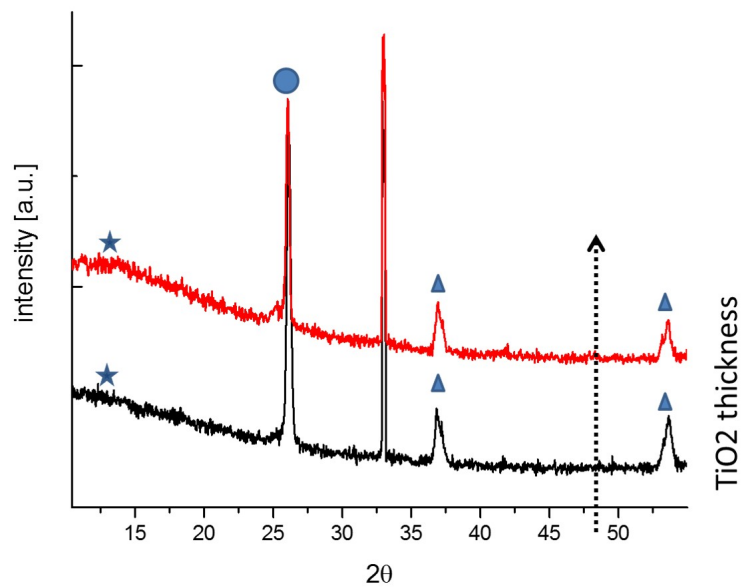
Figure 3.27: XRD spectra of the sample grown on TiO_2 coating of 5 (black spectrum) and 10nm (red spectrum). Both samples are grown at $T_{max} = 700$°C. MoS_2 peaks are marked with stars , MoO_2 ones with triangles and molybdenum titanium oxide with dots.

control and coating uniformity.

A coating thickness of $10nm$ was used since Mo can be itself a precursor for MoS_2 formation. It was observed from our previous experiments that a thick coating is required for the desired protection functionality.

A set of catalyst deposition tuning T_{max} and $T_{entrance}$ was performed. This was done in order to observe if these parameters influence the growth morphology also on the modified substrate.

A collection of the SEM images of the grown samples is reported in figure 3.28.
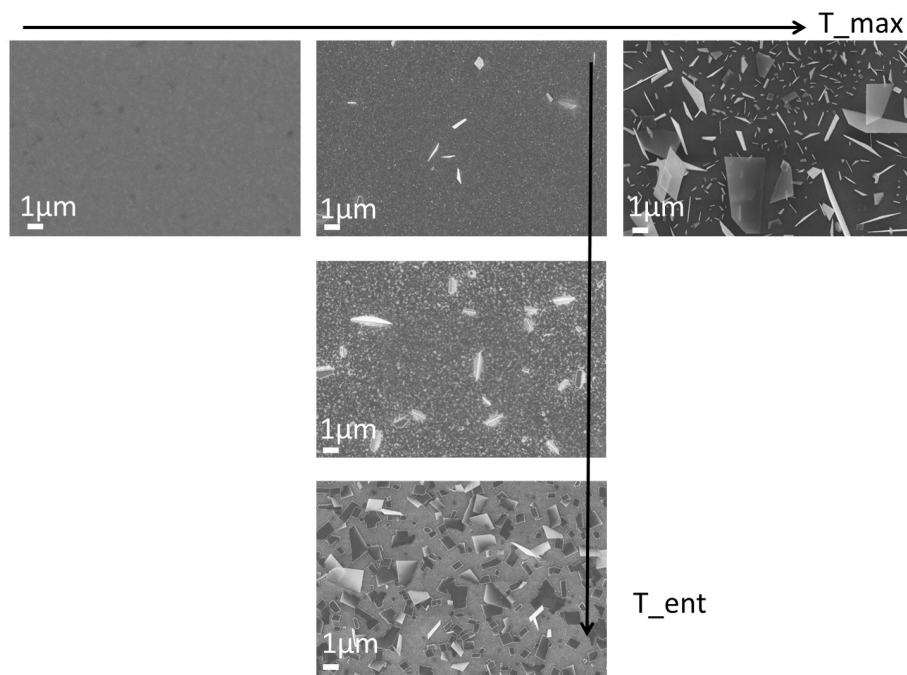
Figure 3.28: Collection of SEM images in function of T_{max} and $T_{entrance}$. From left to right T_{max} =665°,700° and 720°C. From top to bottom $T_{entrance}$ =605°, 615° and 625°C. Other parameters: $H_2S = 20sccm$ $H_2 = 5sccm$ and $t_{growth} = 10min$. The Si substrate orientation is <100>.

Figure 3.28 shows that the material starts to growth with a detectable amount only over a threshold value of $T_{max} \approx 700°C$.

Moreover, increasing T_{max}, a dramatic increase of vertical nanoflakes structures it is observed .

Similar to bare Si substrate, we associate the increase of vertical structures to the increase in MoO_3 evaporation, associated with the higher temperature. The oxide starts to growth at the surface with nanoflakes morphology before being sulfurized by the incoming sulphur precursor.

Furthermore, it is observed that also $T_{entrance}$ has a relevant role in the

catalyst growth morphology. In fact, increasing this value, an abrupt increase in density and length of the grown nanoflakes is observed.

The observed growth morphology on *Mo* coating is similar to the one obtained on bare Si substrate, reported in function of T_{max} and $T_{entrance}$ in figures 3.2 and 3.3.

It is interesting to note that , eventhough high $T_{entrance}$ and T_{max}, both given rise to nanoflakes, their orientation with respect to the substrate is different.

A better visual impact of this difference is given by the SEM cross section images reported in figure 3.29.

High T_entrance   High T_max
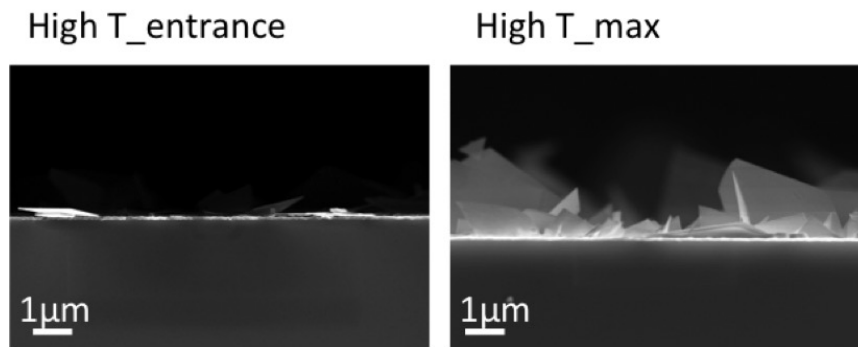
Figure 3.29: Cross section images of the samples grown at $T_{entrance} = 625°C$ and $T_{max} = 700°C$ (on the left) and at $T_{entrance} = 605°C$ and $T_{max} = 720°C$ (on the right). Other parameters: $H_2S = 20sccm$ $H_2 = 5sccm$ and $t_{growth} = 10min$. The Si substrate orientation is <100>.

The reason of this different orientation is not clear yet.

To understand which parameter stimulates vertical alignment it would be interesting to growth with $T_{entrance} = 625°C$ and $T_{max} = 720°C$. This experiment could clarify if verticality is due to 20°C more in T_{max} which lead to an higher amount of MoO_3 vapor, or to the lower sulphur vapor amount in the earlier stage of growth promoted by the higher $T_{entrance}$.

Raman spectroscopy and XRD were performed on these samples.

Raman spectra are reported in figure 3.30, as a function of $T_{entrance}$ and T_{max}.

MoS_2 modes appear for all analyzed samples regardless of $T_{entrance}$. Moreover a small decrease in the modes frequency gap is observed for the samples with the lowest entrance temperature value ($T_{entrance} = 605°$). This observation is confirmed by SEM analysis, since very thin nanoflakes were observed in this samples. An high magnification image is reported in figure 3.31.
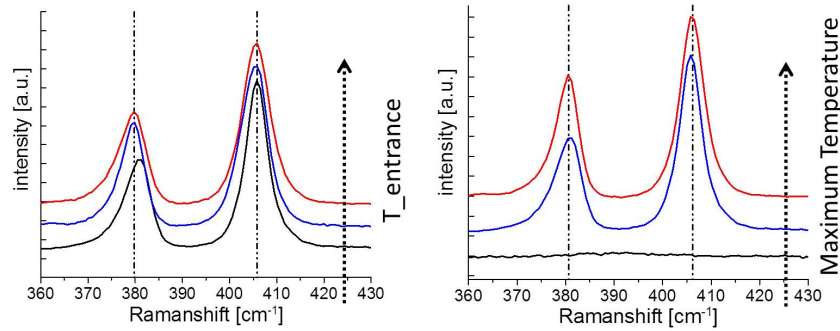
Figure 3.30: Raman spectra compared in function of T_{max} (on the right) and $T_{entrance}$ (on the left). Variation in maximum temperature: T_{max} =665°, 700° and 720°C. Variation in entrance temperature: $T_{entrance}$ =605°, 615° and 625°C. Vertical manipulations of the spectra are done to make easier the comparison. Other parameters: $H_2S = 20sccm$ $H_2 = 5sccm$ and $t_{growth} = 10min$. The Si substrate orientation is <100>.
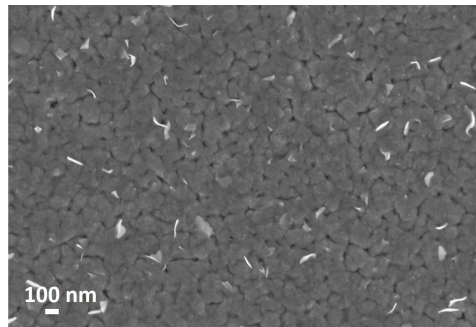
Figure 3.31: SEM image of sample grown at $T_{max} = 700°C$, $T_{entrance} = 605°C$, $H_2S = 20sccm$ $H_2 = 5sccm$ and $t_{growth} = 10min$. The Si substrate orientation is <100>.

On the other hand, absence of MoS_2 feature exist below a threshold temperature ($\approx 700°C$).

No relevant shift in the frequency gap is observed tuning T_{max}.

XRD spectra are reported in figure   3.32 as a function of T_{max} and $T_{entrance}$.

Increasing $T_{entrance}$ the amount of detected MoO_2 increases, which grows with a really high crystallinity in monoclinic phase as attested by the high intensity of the peaks at 18°,26° and 37°. Furthermore, increasing $T_{entrance}$ an increase in MoS_2 peak intensity at 14° is observed.

The second comparison shows a sharp increase in MoS_2 peak intensity at 14° as T_{max} is increased . Moreover, also this analysis shows that a certain temperature threshold ($\approx 700°C$) must be overcome to have MoS_2 growth
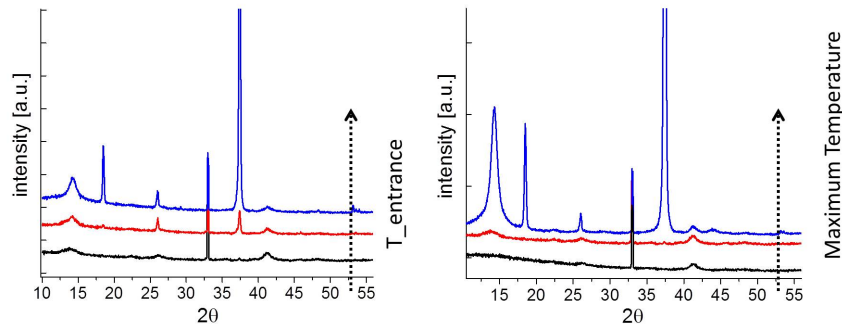
Figure 3.32: XRD spectra compared in function of T_{max} (on the right) and $T_{entrance}$ (on the left). Variation in maximum temperature: T_{max} =665°, 700° and 720°C. Variation in entrance temperature: $T_{entrance}$ =605°, 615° and 625°C. Vertical manipulations of the spectra are done to make easier the comparison. Other parameters: $H_2S = 20sccm$ $H_2 = 5sccm$ and $t_{growth} = 10min$. The Si substrate orientation is <100>.

on this substrate. Increasing T_{max} the typical MoO_2 peaks rise up in intensity and sharpness.

It is important to underline that in all spectra another peak at 41,1° is present.

This is associated with [210] *molybdenum silicide* formation (Mo_3Si, reference spectra reported in *appendix B*).

Due to the high intensity of MoO_2 peaks a further sulfurization step was performed in order to decrease the oxide amount at the surface.
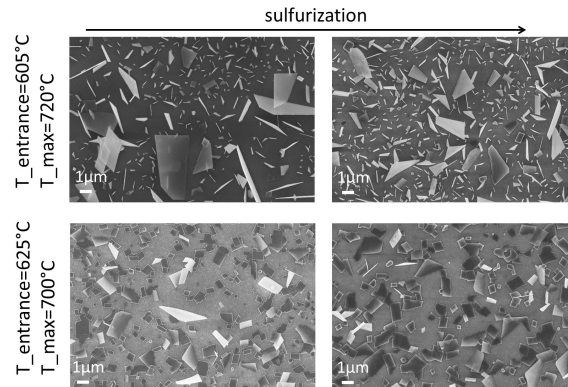
Figure 3.33: SEM images of the samples before and after the sulfurization step. At top, sample grown at:$T_{entrance} = 605°C$ and $T_{max} = 720°C$. At bottom,sample grown at: $T_{entrance} = 625°C$ and $T_{max} = 700°C$. Other growth parameters: $H_2S = 20sccm$ $H_2 = 5sccm$ and $t_{growth} = 10min$. The Si substrate orientation is <100>.

The sulfurization procedure, which is the same performed on sample grown on bare Si, is described in *Atmospheric pressure chemical vapour deposi-*

tion from chapter 2.

I did this procedure only on the 2 samples grown at the highest $T_{entrance}$ and T_{max}, since these ones showed the highest MoO_2 peaks intensity in the XRD analysis. SEM images of these samples grown at $T_{entrance} = 625°C$ - $T_{max} = 700°C$ and $T_{entrance} = 605°C$ - $T_{max} = 720°C$ before and after sulfurization are reported in figure 3.33.

In both samples, the architecture of the catalyst is not modified by the sulfurization step.
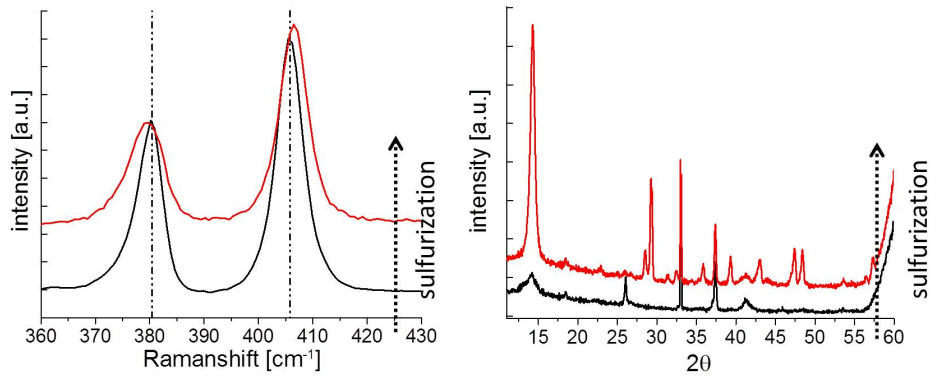
Figure 3.34: Raman and XRD spectra of reference sample before and after the sulfurization.

Raman and XRD analyses were repeated after the sulfurization step.

I report reference spectra before and after the sulfurization in figure 3.34. From Raman comparison is possible to observe a slight increase in frequency gap of MoS_2 modes after the sulfurization . This phenomenon is due to an increase of MoS_2 thickness after sulfurization was, as previously shown in the HRTEM analysis.

XRD comparison shows an increase in the intensity of the peak referred to MoS_2 hexagonal phase at 14°. Moreover,it is observed an intensity decrease of the peak at 26° referred to MoO_2. The XRD analysis after sulfurization shows 7 new peaks , all referred to *molybdenum silicides*.

This phenomenon means that an double heating cycle is required to have a complete reaction of the applied coating with the Si underneath to form crystalline silicide.

3.2 Photoelectrochemical charcaterisation of the lab-scale photocathodes

This section reports on the photo-electrochemical activity of the $MoS_2 - Si$ based photocathodes, prepared with the all the different types of samples described in *Growth study and modulation*. Details on the electrochemical set-up, characterisation procedure and parameters used to classify the samples are found in *electrochemical characterisation* section from chapter 2.

Bare p-type Si pieces (planar and micro-structured) without any catalyst were tested as references. Figure 3.35 shows the obtained characteristic I-V curves obtained under $1Sun$ illumination conditions.
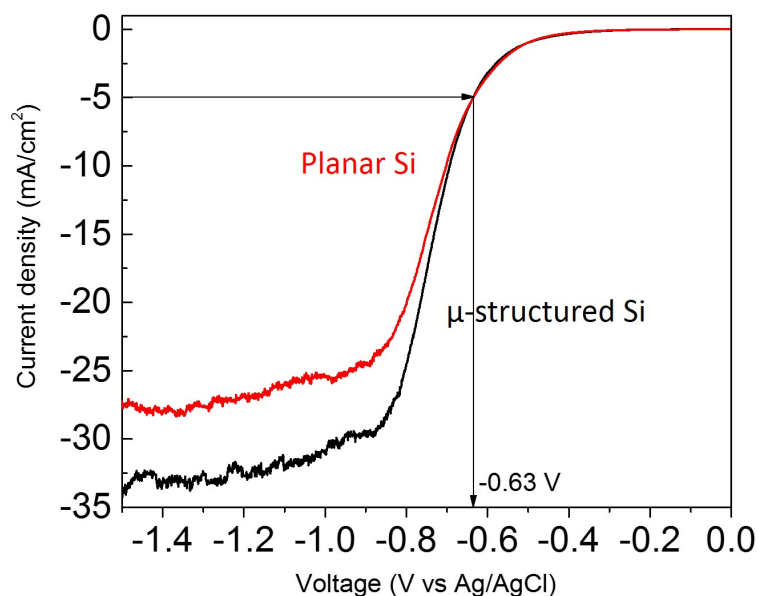
Figure 3.35: I-V curve of bare uncatalysed Si samples.

Using our classification (explained in detail in section *Photoelectrochemical test* from chapter 2), the current density reaches a value of $-5mA/cm^2$ at a voltage of $-0, 63V$ for both reference curves.

At $V = -0.9VvsAg/AgCl$, photo-current saturates at a value of -24 and $-30mA/cm^2$, for planar and micro-structured Si, respectively. The improved saturated photocurrent is a consequence of better light harvesting given in the micro-pillars array.

It must be noted that reversible hydrogen evolution (RHE) reaction in a Pt electrode occurs at $-0.220mVvsAg/AgCl$ at this pH. The higher over-potential respect to Pt is an indication of the poor catalytic properties of Si surface. Even all the gain given by illumination is not enough to spontaneously reduce protons. This means that an external source of potential is

needed when using bare p-Si as photocathode.

The coupling of the surface to a catalyst should improve this situation, by shifting the I-V curve towards more positive potentials.

Unfortunately, we initially observed the opposite trend for our as-grown $MoS_2 - Si$ based samples. All as-grown samples were systematically tested and compared to reference performance.

An example of PEC performance of three representative $MoS_2 - Si$ samples is shown in figure 3.36.

Three main observations can be made:

- low current density

- a systematic shift towards more negative potentials

- worsened fill factor
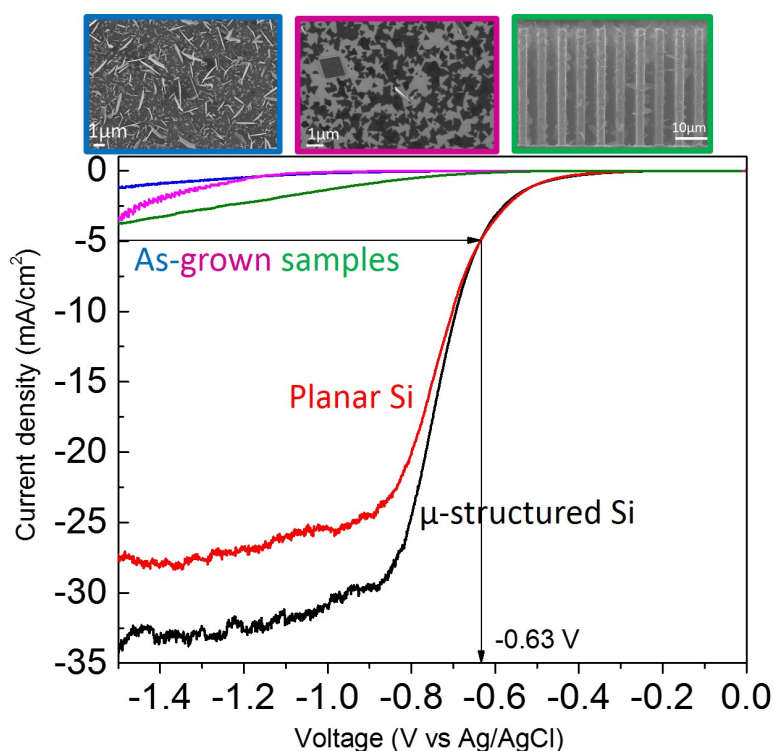
Figure 3.36: I-V curves of samples with nanoflakes (blue curve)and $2D$ planar structures (purple curve) catalyst morphologies and grown on micro pillars structures. The samples curves are compared with reference performance. All the curves are obtained under $1Sun$ of illumination.

It is clear that electron injection to the electrolyte is strongly limited after MoS_2 growth. Several factors could account for such decreased perfor-

mance. It could well be that the interface between Si and MoS_2 (or MoO_2) is not perfectly ohmic. Also, since the growth is performed in an oxidizing atmosphere, Si may have oxidized during MoS_2 growth. The employment of MoO_3 as molybdenum precursor leaves its oxygen atoms at the Si surface once activated, where they can induce a surface oxidation.

Due to the unlikelihood of substituting MoO_3 with an oxygen free precursor, two approaches were attempted to overcome this issue:

- To etch the sample after growth with buffered HF

- To deposit a protective coating on p-type Si before the deposition

A detailed description of the used procedures and the obtained results applying these two ideas are reported in the following subsections.

3.2.1 Oxide removal after catalyst deposition

The idea to etch the sample after the catalyst deposition is an effective and simple way to remove the Si oxide formed during the AP-CVD step without removing the catalyst itself, since MoS_2 is resistant to HF.

SEM images before and after the etching step (figure 3.37) show that MoS_2 nanoflakes are not removed by the acid bath.
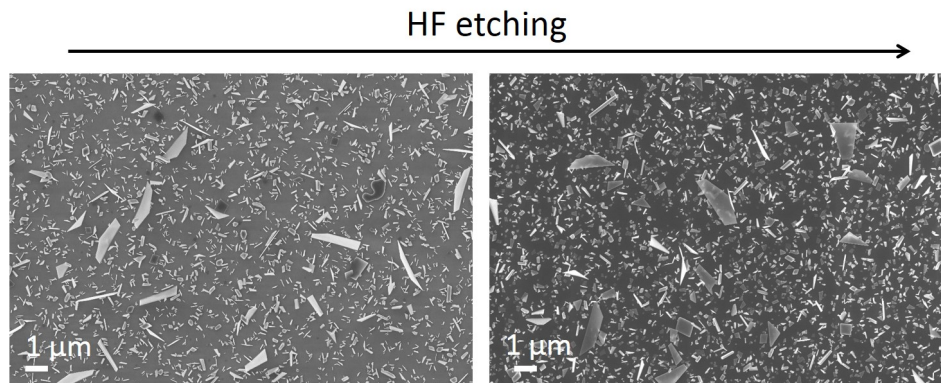
Figure 3.37: SEM images of the same sample before and after HF etching in buffered HF for 1 min. Growth parameters: $T_{max} = 700°C$, $T_{entrance} = 605°C$, $H_2S = 15sccm$, $H_2 = 15sccm$, $t_{growth} = 10min$.

I-V curves of as-grown and HF etched samples with nanoflakes and $2D$ planar catalyst morphologies plus one grown on micro-pillars structure are reported in figure 3.38 .
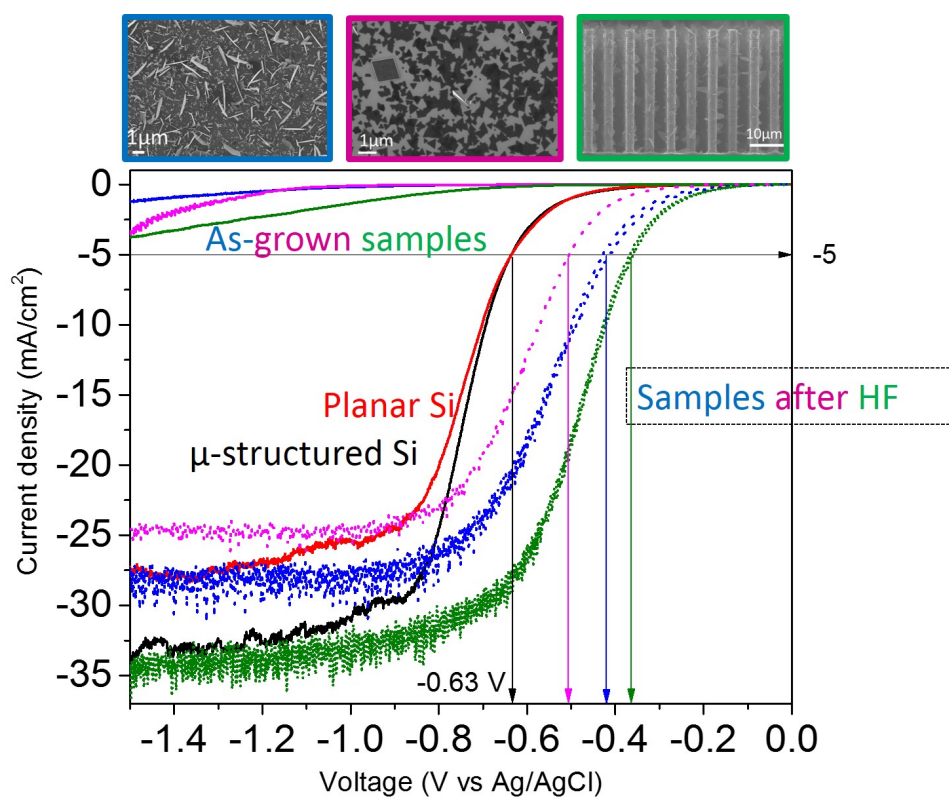
Figure 3.38: I-V curves of samples with nanoflakes (blue curve)and $2D$ planar structures (purple curve) catalyst morphologies and grown on micro pillars structures. The dots line are referred to the same samples after HF etching. The samples curves are compared with reference performance. All the curves are obtained under $1Sun$ of illumination.

The photo-cathode response is clearly improved by HF-etching step.

What's more, by comparing the outputs of the etched samples (dot curves) with the bare Si references (red and black curves), we observe a shift of the electrical characteristic towards higher potentials. This improvement is quantified comparing overpotentials at $-5mA/cm^2$:

reference	2D planar morphology	nanoflakes morphology	grown on $\mu pillars$
-0.63	-0.5	-0.41	-0.36

All the reported onset potential values are in V vs $Ag/AgCl$.

The maximum improvement was obtained growing the catalyst on $\mu pillars$ Si structures, shifting V_{onset} of $\mid 0.27 \mid V$ vs $Ag/AgCl$. We attribute this improvement to the catalytic properties of MoS_2 structures. The sharp improvement of the output after HF etching proves that the issue was related to the presence of Si oxide.

Moreover, the samples with nanoflakes morphology shows a better decrease in estimated overpotential and an higher photocurrent at saturation point than the one with $2D$ planar structures. This gain could be related to nanoflake structure which is supposed to expose more active sites and to guarantee an better charges transport. On the other hand, we suppose that vertical alignment doesn't reduce the Si light absorption as the $2D$ planar structure.

Next step is to test the sulfurized samples etched with HF, since our analysis clearly showed an in increase of MoS_2 during sulfurization step.

3.2.2 Protection coating

The second approach to prevent silicon oxidation is to protect the substrate with a thin coating before growth. The chosen coating are: *Ti*, *TiO$_2$* and *Mo*.

The catalyst growth on these coatings has been discussed in the previous section *Growth study and modulation*. In this section, I report only the reasons of these choices and relevant results in the photoelectrochemical caracterisation.

These coatings were chosen after a material selection. The considered requirements in the selection are :

- To be stable at high temperatures ($600° - 750°C$)

- To be stable in acidic environments (electrochemical test is done at $pH = 0$)

- To enable electron transfer from p-Si to water

- To be transparent

In order to ensure the injection of electrons to the electrolyte, we need a material that has a workfunction more negative than Si. If the coating absorbs visible light, the layer must be thin enough so that most photons reach the Si underneath. At the same time, the thin coating must be thick enough so that conformally protects the Si. During MoS_2 growth, the substrate is exposed to temperatures up to $750°C$. Interdiffusion of Silicon during heating and hydrogen embrittlement during the electrochemical tests, must be also kept into account.

We chosen *Ti* and *Mo* because they form silicide compounds when brought in contact with Si at high temperatures. This alloying has been widely used in industry to form ohmic contacts.

On the other hand, *TiO$_2$* is a wide bandgap semiconductor that has been already used as Si protection coating for PEC applications.

Before deposition of the coating, p-Si substrates were HF etched to remove any native oxide.

Ti coating was applied with different thicknesses ($1, 2, 4$ and $5nm$) and it was tested both annealed and not. Reference I/V curves are reported in figure 3.39
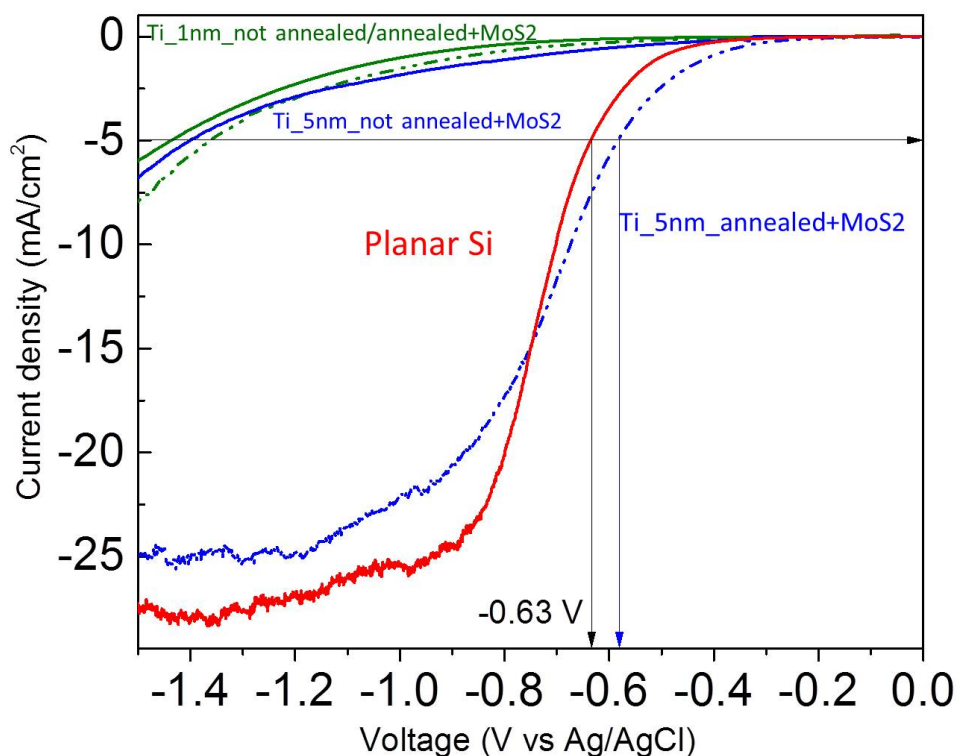
Figure 3.39: I-V curves of samples with $5nm$ of Ti (blue curve)and $1nm$ of Ti (green curve) . The dots line are referred to the same samples with RTA step before the catalyst deposition. The samples curves are compared with reference performance. All the curves are obtained under $1Sun$ of illumination.

From the comparison it is clear that a thick coating ($5nm$) is required to protect the Si from oxidation during AP-CVD with this material. Moreover, this coating must be annealed before the catalyst deposition. With $5nm$ of annealed Ti, we observed a small shift of V_{onset} towards higher potential, with a measured gain of of $\mid 0.05 \mid V$ vs $Ag/AgCl$. However, a worst fill-factor with a smaller photocurrent value at saturation and a rapid deterioration of the response was attested after prolonged cyclic voltammetry tests. For these reasons we concluded that Ti coating is not suitable for this application.

TiO_2 coatings were applied by ALD with thicknesses of 5 and $10nm$.

The electrochemical analysis shows a very low photocurrent output for this batch of samples. Moreover, from cyclic voltammetry tests it was observed a very high rate of degradation of the overall surface cycle after cycle. Reference I/V curve is compared with the bare Si reference one in figure 3.40 .
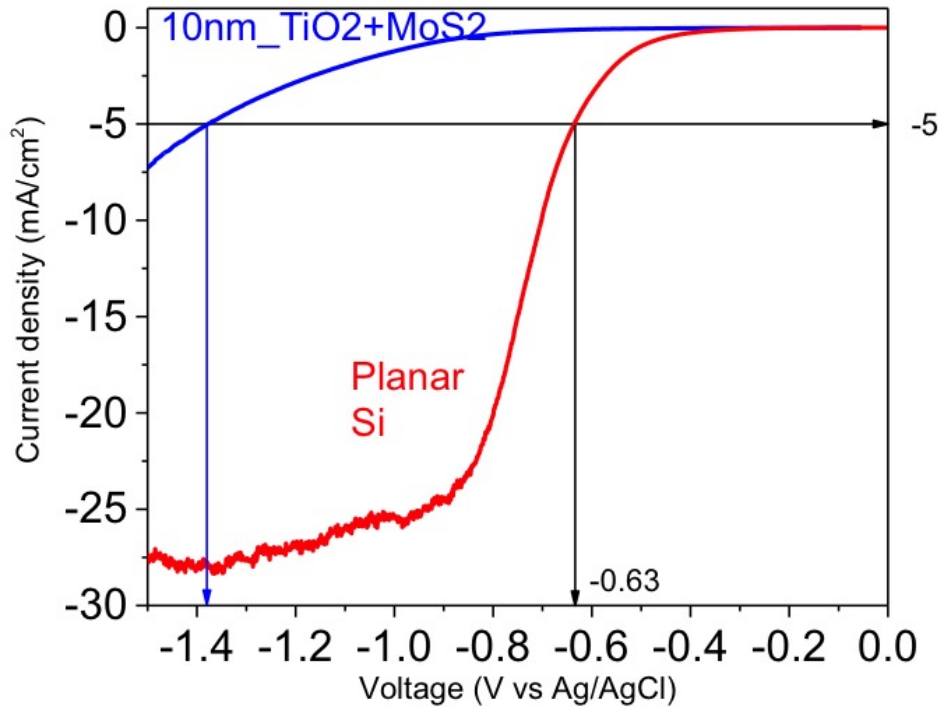
Figure 3.40: I-V curve of sample with $10nm$ of TiO_2 (blue curve). The sample curve is compared with reference performance (red curve). All the curves are obtained under $1Sun$ of illumination.

From comparison it is clear that this coating, even with $10nm$ of thickness does not protect Si from the oxidation during AP-CVD. However, TiO_2 in the rutile phase has already been proved to be a good protection coating for photoelectrochemical applications. Therefore, we suppose i that this low output is due to the non-crystallinity of the coating, as proved by dedicated XRD analysis presented in section *Growth study and modulation*. We concluded that amorphous TiO_2 is not suitable to be applied as protection coating against Si oxidation in our AP-CVD process.

Mo coating was applied with only one thickness ($10nm$), tuning the deposition parameters T_{max} and $T_{entrance}$.

From the photoelectrochemical test, we observed a very small current gain under illumination. We related this result to a reduction band bending promoted by the coating thickness. This phenomenon can avoid the semiconductor-liquid junction formation and the consequent splitting of the photogenerated carriers. However, a drop of current at higher potentials was observed in the I/V curves obtained in dark . Moreover, the potential at which this current starts to drop tune in function of the deposition parameters as reported in figure 3.41.
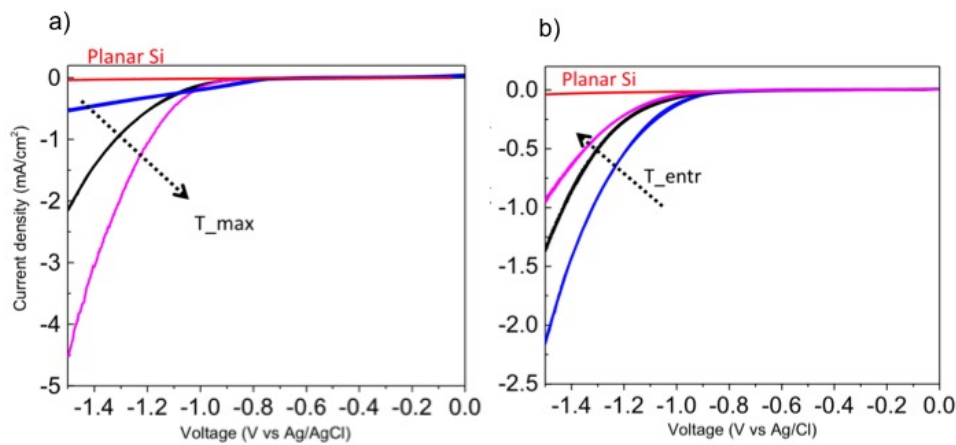
Figure 3.41: a)I-V curves of samples with $10nm$ of *Mo* grown at T_{max} of 665° (blue curve), 700° (black curve) and 720°C (purple curve).b) I-V curves of samples with $10nm$ of *Mo* grown at $T_{entrance}$ of 605° (blue curve), 615° (black curve) and 625°C (purple curve).The sample curve is compared with reference performance (red curve). All the curves are obtained in dark.

From the figure, we observe that at higher T_{max} and lower $T_{entrance}$ a drop in current values occurs at higher potentials: this suggests an enhanced catalytic activity.

Referring to SEM images reported in figure 3.28, we observed an increase in the catalytic activity as it increases the amount of nanoflakes on the substrate surface. This happen at high T_{max}.

On the other hand, at high $T_{entrance}$ we increase the oxide amount. In this case a lower catalytic activity is observed.

Due to the observed good activity at high T_{max} , more efforts were done in this direction.
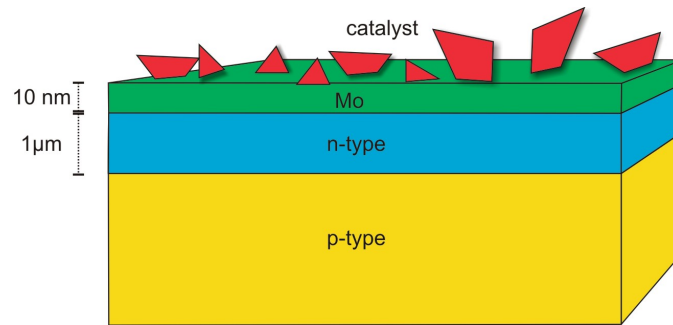
Figure 3.42: Schematic representation of the designed photocathode based on a
$p - n$ junction. The light is supposed to be shined from the top.

Since the main problem is supposed to be a flattening of the semiconductor band edges due to the excessive thickness of the coating, we tried to overcome the need of semiconductor-liquid junction, applying the $10nm$ of *Mo* coating on a Si based p-n junction.

Using a p-n junction the built in voltage needed to split the photogenerated carriers is given by the semiconductor p-n junction itself.

This p-n junction was created starting by a p-doped Si wafer full RCA cleaned and creating the n-side by phosphorous diffusion doping at 850°C for 15 minutes (process done by Jelena Vukajlovic Plestina, LMSC,EPFL). A schematic representation of this new device prototype is reported in figure 3.42.

After a surface etching performed with *HF* to remove any traces of oxide, *Mo* coating was deposited with a thickness of $10nm$ by e-beam evaporator, maintaining the same conditions of the previous batch of samples. Secondly the catalyst was applied by AP-CVD, using $T_{max} = 720°C$, since catalyst grown at this condition has shown the best activity. A further sulfurization step was performed, always with the procedure reported in section *Atmospheric pressure chemical vapour deposition* from chapter 2.

I/V curves obtained in dark and under $1Sun$ of illumination for reference sample sulfurized and not are reported and compared in the figure 3.43.

From the figure a sharp difference between the samples not sulfurized and sulfurized is observed both for the dark and under illumination curves. We have observed in XRD analysis the appearance of more peaks referred to molybdenum silicide after the heating that occurs in sulfurization step (refer to figure 3.34) . For that reason, this great difference in I/V curves could be due to a lower metallic character of the surface after the complete alloying with the substrate.
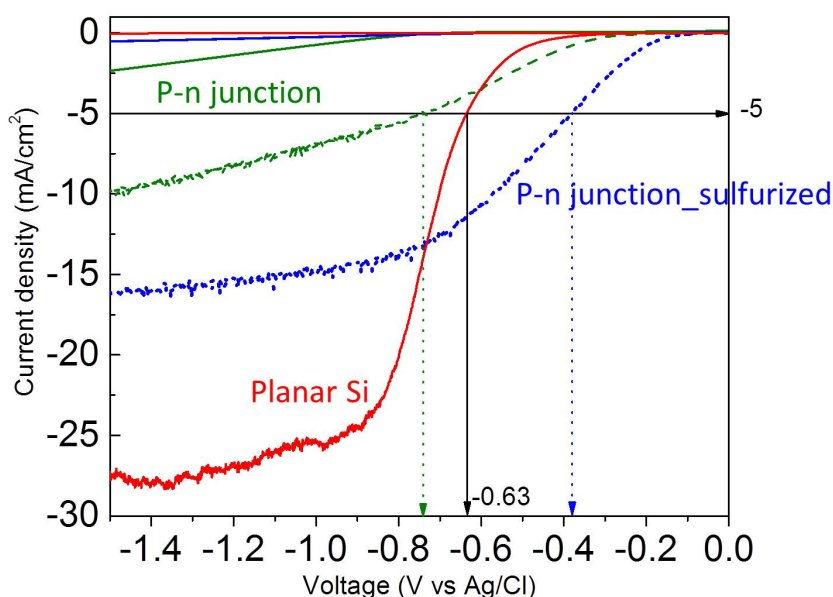
Figure 3.43: I-V curves of samples made of p-n junction coated with $10nm$ of Mo and with MoS_2 catalyst grown at $T_{max} = 720°$ and $T_{entrance} = 605°$. Blue curve are for sufurized sample, green for not sulfurized one. Dashed curves are obtained under $1Sun$ of illumination. The samples curves are compared with reference performance in dark and light (red curves).

Moreover, sulfurized sample shows a great improvement in $V onset$ under illumination, with a gain of $| 0.25 | V$ vs $Ag/AgCl$ respect to the reference bare Si. However, compared to the reference performance a decreased of $\sim 10mA$ in photocurrent value at saturation point is observed. This is due to the limited absorption of the Si, promoted by the coating application.

In this regard, It could be interesting to try to apply a thinner Mo coating ($5nm$) and observe if it can increase the Si absorption continuing to protect it from oxidation.

3.3 Summary

In the first part of this chapter, I have reported the results concerning the study and the modulation of MoS_2 catalyst growth on p-type Si substrate.

An effective change in catalyst morphology from $2D$ planar structures to vertical aligned nanoflakes is observed tuning the temperature parameters (T_{max} and $T_{entrance}$) in the deposition process. On the other hand, changing gas flows/ratio (H_2 and H_2S), $time_{growth}$, Si substrate crystallographic orientation and morphology, no changes in the grown catalyst morphology are observed. XRD analysis has revealed the presence of MoO_2 only in

nanoflakes structures, suggesting us a core-shell MoO_2/MoS_2 structure.

Further experiments (i.e sulfurization step) and analyses (i.e. STEM and EELS) on nanoflakes confirm the presence of an oxide core with an inhomogeneous sulphur amount localized at lateral edges, which tends to propagate towards the core of the nano-structure during sulfurization process.

After that, I have reported the catalyst growth study done on planar <100> Si substrates functionalized with thin coating of *Ti*, TiO_2 and *Mo*. In this regard, we have observed an extremely different catalyst growth morphology, due to the modified substrate surface. A nanoflake morphology, similar to the one achieved on bare Si, is observed only for *Mo* functionalized substrate.

In the second part of this chapter, I have reported the results concerning photoelectrochemical test of the lab-scale photocathodes made with the AP-CVD grown samples.

As-grown samples have readily shown limited photocurrent, worsen fill factor and a systematic shift towards more negative potentials. We have related these limitations to a Si substrate oxidation during the catalyst growth.

To overcome this issue, I have etched the as-grown samples with HF to remove the silicon oxide or we have functionalized the substrate before the catalyst growth to prevent the Si oxidation.

I have shown that after HF etching the photocathode response is fairly improved, with a systematic decrease in overpotential due to MoS_2 catalyst presence. The comparison between different catalyst morphologies shows a greater decrease in overpotential given by nanoflakes structures than $2D$ planar structures. The greatest overpotential reduction observed is achieved catalysing p-type Si micro-pillar arrays with MoS_2 nanoflakes.

The functionalisation of planar <100> Si surface with *Ti* and TiO_2 have not shown improve of the photocathode response. On the other hand, a good catalyst activity was observed for samples grown on *Mo* functionalized substrates. However a limited photocurrent has been reported due to the *Mo* reflection and to the Si band flattening. We have solved this problem applying the *Mo* coating and the MoS_2 catalyst on a Si p-n junction. With this buried junction, enhanced overpotential reductions has been achieved.

Chapter 4

Conclusion and outlooks

In this work we have performed and studied direct synthesis of MoS_2 nanostructures, catalytically active for HER, synthetized by AP-CVD on Si substrate with different crystallographic orientations (<100> and <111>), morphologies (planar, micro- and nano-pillars arrays) and functionalization thin coatings (*Ti*, *TiO$_2$* and *Mo*). Tuning the growth parameters, and in particular T_{max} and $T_{entrance}$, we are able to modulate the catalyst morphology from 2*D* planar to vertical nanoflakes structures with absolute reproducibility. Our one is the first example of direct *one step* synthesis of MoS_2 vertical aligned nanoflakes. We have assessed that nanoflakes structures start to growth as MoO_2 on the Si substrate, being afterward sulfurized starting by the edges of the nanostructure. A further study of nanoflake structure is planned to better understand this interesting mechanism of sulfurization.

Secondly, we have observed an HER overpotential decrease correlated with AP-CVD grown *MoS*2 catalyst application. A larger overpotential decrease after MoS_2 nanoflakes morphology application is observed respect to 2*D* planar morphology one. This higher activity can be related to the potential higher electron mobility in vertical structures respect to planar ones. To confirm this hypothesis, electrical measurements could be performed on nanoflakes. Moreover, first measurements performed on these samples with *scanning electrochemical microscope* (SECM) show the possibility to detect the locally the catalyzed surface activity. Therefore, SECM could be use to understand which are effectively the active MoS_2 grown structures, leading us to selectively study only the more promising.

Appendices

Appendix A

Semiconductor-Electrolyte interface

An understanding of the *semiconductor-electrolyte interface* is crucial for the design and realization of a PEC cell, since it is in this part that the chemical reactions take place, resulting it to be the heart of the conversion principle.

First of all, it is useful to describe separately the energetic scheme of the semiconductor material p-doped and of the electrolyte , as reported in the following figure.

The band structure of the p-type semiconductor is defined by the valence (VB) and conduction (CB) bands, which are separated by the energy band gap (E_g). In p-type semiconductor, the chemical potential or Fermi level (E_f) is slightly above the VB edge   [34].

The electrolyte has energy levels related to the redox couple in the solution. The elecrolyte solution is composed by ionic species, acceptors (Ox) and donors (Red), which give to the electrolyte the ability to transport charge. The energy values of the solution states are not fixed, because in the bulk electrolyte there is a dynamic exchange between the redox-active species: for this fluctuations the density of states are represented with Gaussian distributions   [31] . The functions which represent the occupied (Red) and empty (Ox) states are:

$$D_{ox} = \exp[-\frac{E - E_{F,redox} - \lambda^2}{4kT\lambda}]$$

$$D_{red} = \exp[-\frac{E - E_{F,redox} + \lambda^2}{4kT\lambda}]$$

Where λ is the solvent reorganization energy for a redox couple. The redox chemical potential or Fermi level ($E_{F,redox}$) is defined as the energy level at which the probability that a state being occupied by an electron is 0.5. A widely accepted equation express the position of the $E_{F,redox}$ versus
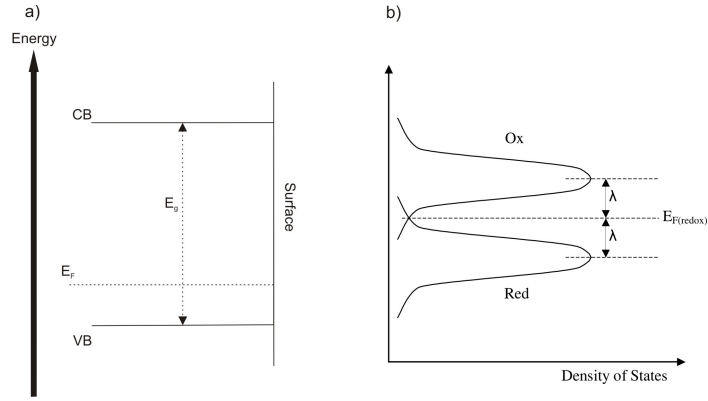
Figure A.1: a) P-doped semiconductor band scheme b) Representation of the redox couple density of state in function of the energy.

the vacuum reference one as:

$$E_{F,redox} = -4.5eV - e_0 E_{redox}$$

Where 4.5 is the scale factor relating the H^+/H_2 redox level to vacuum and e_0 is the electron charge. Here it is evident that $E_{F,redox}$ has a dependence on the electrochemical potential of the electrons in the redox electrolyte (E_{redox}). The latter is properly described by the *Nernst's equation*:

$$E_{redox} = E_{redox}^0 + \frac{RT}{nF} \ln\left[\frac{c_{ox}}{c_{red}}\right]$$

The previous equation states the dependence of the electrochemical potential (E_{redox}) to the standard electrochemical potential (E_{redox}^0), that it is given for the selected redox couple, and to the concentrations of the oxidized (c_{ox}) and reduced (c_{Red}) species in the solution. As a consequence, being the redox couple fixed by the desired chemistry, only the concentrations of the oxidized and reduced species can be changed to tune the E_{redox} value, in order to modify on occurrence the $E_{F,redox}$ one and so the semiconductor-electrolyte interface energetics. In other words, the electrochemical potential can be adjusted simply changing the pH of the solution.

In such case, it has been shown that tuning the pH doesn't always modify the semiconductor-water interface energetic. The reason, lies on the covering of the semiconductor surface by hydroxyl groups which protonate/deprotonate as the pH changes. As a result, the bands show also a pH dependence in unison with that of redox electrochemical potential [21].

For this reason, in a PEC cell design the choice of the semiconductor material, as well as the functionalization of its surface, is dramatically important in interface energetics. When a p-type semiconductor is brought
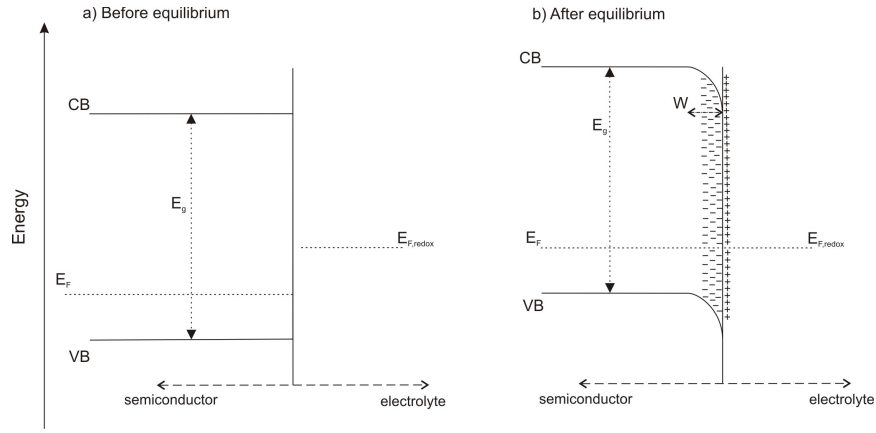
Figure A.2: a) Semiconductor-electrolyte interface before the equilibration b) Semiconductor- electrolyte interface after that the equilibrium is established.

in contact with an electrolyte that contains a redox couple, without the application of any external bias, a flow of charges is established between the redox states and the semiconductor. Once the Fermi levels are equilibrated ($E_F = E_{F,redox}$), a downward band bending will exist at the semiconductor surface.

The total band bending and its extension depends on the redox couple and doping density of the semiconductor [31, 36] . A schematic representation of the energetics equilibration is reported in the figure.

The equilibration is provided by a depletion of majority carriers in the semiconductor that leave a layer of ionized acceptors behind (depletion layer). This negative charge is compensated by the formation of a thin bilayer at the electrolyte next to the interface, also called Helmholtz double layer. At the Helmoltz layer ions coming from the solution are adsorbed at the semiconductor surface. Beyond the depletion region and Helmoltz layer, that have widths between $10 - 1000nm$ and $0.4 - 0.6nm$ respectively, electrical neutrality is maintained. Due to the presence of fixed charges, a built in voltage arises (V_{SC}) with a corresponding electric field. This electric field is mainly in the semiconductor, since the width of the charge accumulation region is much larger than the Helmoltz layer. A quantification of the potential drop in this region is given by the Poisson equation:

$$V_{sc} = -(\frac{e_0 N_A}{2\varepsilon_S})W^2$$

Where e_0 is the electronic charge, ε_S is the static dielectric constant of the semiconductor, N_A is the Avogadro's number and W is the width of the depletion region, which is sensible to the semiconductor level of doping (increasing the doping level it decreases W).

To determine the band bending, the simplest approachis through the system Capacitance. The Mott-Schottky equation, which is derived from the Poisson's equation, relates the semiconductor depletion layer capacitance (C_{CS}) with potential.

$$\frac{1}{C_{SC}^2} = \frac{2}{N_A e_0 \varepsilon_S}[(V - V_{fb}) - \frac{kT}{e_0}]$$

Here V_{fb} is called *flat band potential*, which is the potential value at which the semiconductor's bands become flat. By measuring V_{fb} and N_A it is possible to obtain the E_F and the positions of CB and VB [18].

Moreover, it is important to underline that at equilibrium, the interface is in a dynamic equilibrium state, where the forward and reverse currents exactly balance each other, so that there is no net current across the interface2.

It must be noted that, in many cases the semiconductor-liquid junction behaviour is not ideal, mainly due to the surface states. In such cases, a more complex modelling is required [31, 4, 29].

Under illumination,the semiconductor material absorbs light with photon energy equal or higher than the band gap energy ($hv \geq E_g$). For an indirect band gap semiconductor the case of Silicon the absorption coefficient can be described by the formula:

$$\alpha = A(hv - E_g)^2$$

From this value it is possible to obtain an important parameter that is the absorption depth ($1/\alpha$), which can be up to $10^4 nm$ for indirect band gap semiconductors as silicon.

Electron-hole pairs are generated upon photon absorption within the absorption depth. However only photocarriers,that are generated within the depletion region plus the diffusion length of minority carriers (L_e), will be separated and effectively do electrical work. The rest will recombine. For a p-type semiconductor the minority carriers are electrons and L_e is given by:

$$L_e = \sqrt{D_e \tau_e}$$

Where D_e and τ_e are respectively the electron diffusion coefficient and life time.

After exciton separation, minority carriers drift towards the solution thanks to the electric field. At the surface, minority carriers are available for the HER, while majority carriers are driven to the rear ohmic contact. Under open circuit conditions and steady state illumination, a surplus of holes exists in the semiconductor rear contact: this decreases the potential difference across the junction, leading to a less pronounced band bending and the splitting of quasi-Fermi levels at the surface.
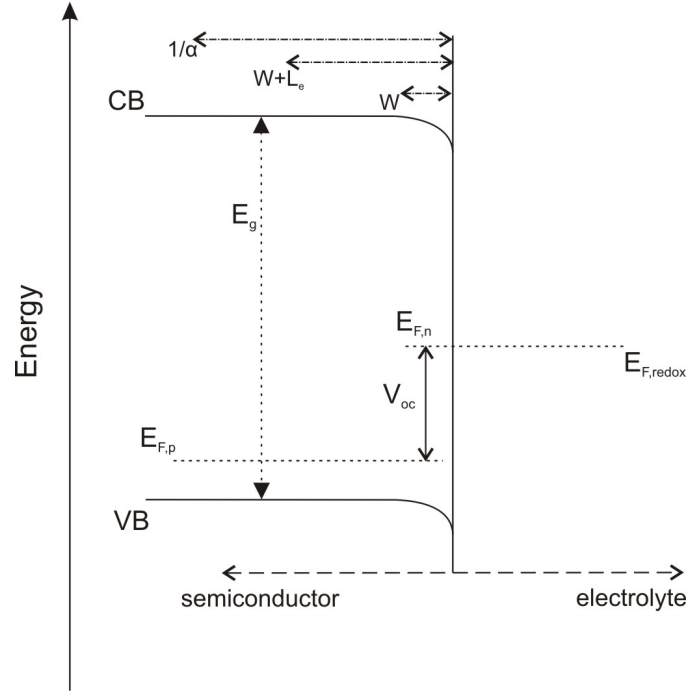
Figure A.3: Semiconductor-electrolyte interface under illumination.

However, not all photo-carriers may contribute to photocurrent, because some of them recombine before reaching the semiconductor surface or the back contact. Recombination can occur with different dominant mechanisms, and decreases the internal quantum efficiency of the conversion process. Under steady state illumination the system is in a quasi-equilibrium state and the earlier equalised Fermi level is splitted in two quasi-Fermi levels, generating a photovoltage.

The current-voltage characteristics of an illuminated semiconductor electrode in contact with a redox electrolyte can be obtained by adding together the majority and the minority current components. The former component is given by the diode equation, and the latter is directly proportional to the photon flux. The resulting net current density is given by [31]:

$$i = i_{ph} - i_0[\exp(-\frac{e_0 V}{kT}) - 1]$$

The minus between the two components of the equation underlines that these ones flow towards opposite sites. In open circuit condition i is equal to zero and from the previous equation is possible to derive the open circuit potential (V_{oc}) expression:

$$V_{oc} \sim \frac{kT}{e_0} \ln(\frac{i_{ph}}{i_0} + 1)$$
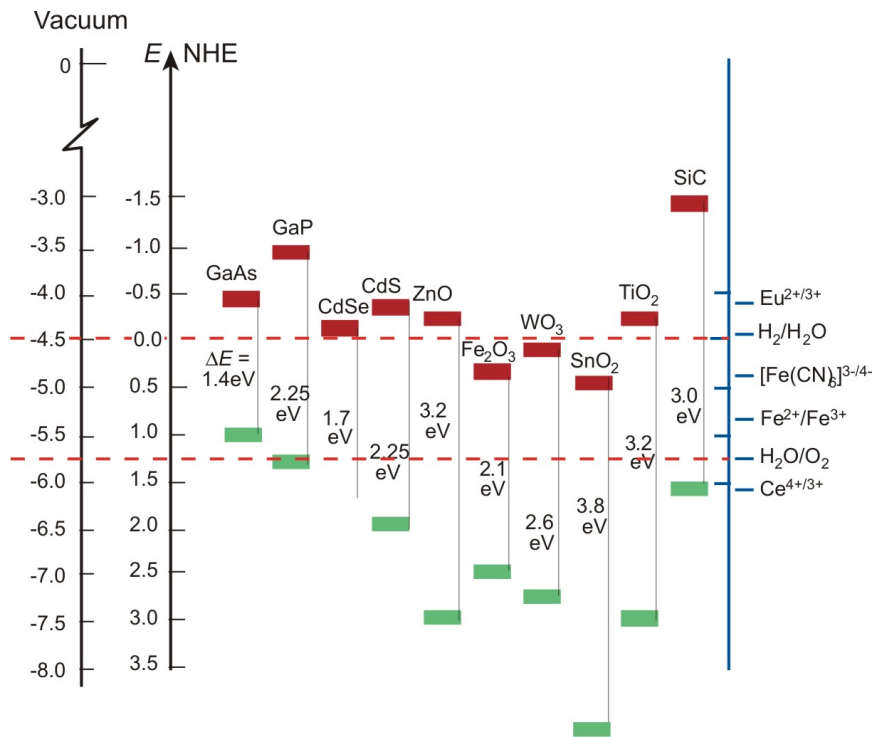
Figure A.4: VB and CB positions of some materials commonly studied for PEC water splitting. Figure used with the authors authorization [19]

This expression states the logarithmic increase of the V_{oc} of the system by increasing the photocurrent (i.e. with light intensity). Therefore in a semiconductor-liquid interface used for PEC systems it is important to have a fast minority carriers kinetic (i.e. large i_{ph}) and at the same time to block majority carrier injection into the electrolyte (which are holes and come from the VB in the p-type semiconductor case).

As reported in figure 3, V_{oc} refers to the degree of splitting between the electron and hole quasi Fermi levels. The maximum splitting achievable is determined by the difference in the workfunction of semiconductor and electrolyte [36, 27].

In figure $A.4$ are reported the band positions of several semiconductor materials with respect to the levels of water reduction and oxidation.

If energetics of the water oxidation/reduction are not favourable according to the semiconductor VB/CB, other reactions may occur, such as semiconductor self-oxidation.

Thus, it is important that the semiconductor material is stable in contact with the electrolyte both in dark and under illumination conditions.

Appendix B

Tables

Recipes used for samples grown on planar Si (both <100> and <111>) without any coating:

Sample name	$H_2[sccm]$	$H_2S[sccm]$	$T_{entrance}[C]$	$T_{max}[C]$	$time_{growth}[min]$
29/07/14	15	5	625	700	10
31/07/14	15	5	600	700	10
05/08/14	15	15	625	700	10
06/08/14	5	15	625	700	10
08/08/14	15	5	615	700	10
12/08/14	15	5	610	700	10
14/08/14	5	15	600	700	10
15/08/14	15	5	605	700	10
19/08/14	5	15	605	700	10
21/08/14	15	15	605	700	10
26/08/14	5	5	605	700	10
27/08/14	15	5	605	700	2
28/08/14	15	5	605	650	10
29/08/14	15	5	605	665	10
02/09/14	15	5	605	665	10
03/09/14	15	5	605	660	10
09/09/14	15	15	605	660	10

Sample name	$H_2[sccm]$	$H_2S[sccm]$	$T_{entrance}[C]$	$T_{max}[C]$	$time_{growth}[min]$
10/09/14	15	15	605	660	10
16/09/14	15	5	605	660	10
17/09/14	15	5	625	660	10
19/09/14	5	15	605	660	10
25/09/14	5	20	605	660	10
21/04/15	15	5	605	660	10
22/04/15	15	5	605	660	20
23/04/15	15	5	605	660	20
24/04/15	5	20	605	660	20
27/04/15	15	5	605	700	20
29/04/15	15	5	605	700	20
30/04/15	15	5	605	700	20
01/05/15	15	5	605	665	10
04/05/15	5	15	605	665	10
06/05/15	15	5	600	600	30

Recipes used for samples grown on Si micro- and nano-pillars array (the only Si crystallographic orientation used is <100>):

Sample name	$H_2[sccm]$	$H_2S[sccm]$	$T_{entrance}[C]$	$T_{max}[C]$	$time_{growth}[min]$
14/10/14	5	15	605	660	10
16/10/14	5	15	605	700	10
17/10/14	5	15	605	680	10
20/10/14	5	15	605	710	10
22/10/14	5	15	605	700	15
23/10/14	5	15	605	700	2
29/10/14	5	20	605	700	10

Recipes used for samples grown on a thin coating functionalized Si <100> substrate :

I report the technical sheet for MoS_2 and MoO_2 respectively used in XRD characterisation.

Sample name	H_2 [sccm]	H_2S [sccm]	$T_{entrance}$ [C]	T_{max} [C]	t_{growth} [min]	coatingtype	thickness [nm]
19/05/15	15	5	605	665	10	Ti	4
21/05/15	15	5	605	665	10	Ti	4
26/05/15	15	5	605	665	10	Ti	2
27/05/15	15	5	605	665	10	Ti	1
28/05/15	15	5	605	665	10	Ti	5
05/06/15	15	5	605	700	10	Ti	1 and 2
10/06/15	15	5	605	665	10	TiO2	5 and 10
15/06/15	15	5	605	700	10	TiO2	5 and 10
19/06/15	5	20	605	700	10	Mo	10
22/06/15	5	20	625	700	10	Mo	10
23/06/15	5	20	605	720	10	Mo	10
24/06/15	5	20	605	665	10	Mo	10
25/06/15	5	20	615	700	10	Mo	10

Name and formula

Reference code: 00-006-0097

Mineral name: Molybdenite-2H, *syn*
Compound name: Molybdenum Sulfide
PDF index name: Molybdenum Sulfide

Empirical formula: MoS_2
Chemical formula: MoS_2

Crystallographic parameters

Crystal system: Hexagonal
Space group: P63/mmc
Space group number: 194

a (Å):   3.1600
b (Å):   3.1600
c (Å):   12.2950
Alpha (°):   90.0000
Beta (°):   90.0000
Gamma (°):   120.0000

Calculated density (g/cm^3):   5.00
Measured density (g/cm^3):   5.06
Volume of cell (10^6 pm^3):   106.32
Z: 2.00

Peak list

No.	h	k	l	d [Å]	2Theta[deg]	I [%]
1	0	0	2	6.15000	14.391	100.0
2	0	0	4	3.07500	29.015	4.0
3	1	0	0	2.73700	32.692	16.0
4	1	0	1	2.67400	33.485	10.0
5	1	0	2	2.50100	35.877	8.0
6	1	0	3	2.27700	39.546	45.0
7	0	0	6	2.04900	44.165	14.0
8	1	0	5	1.83000	49.786	25.0
9	1	0	6	1.64100	55.992	4.0
10	1	1	0	1.58100	58.316	12.0
11	0	0	8	1.53800	60.112	12.0
12	1	0	7	1.47840	62.803	2.0
13	2	0	0	1.36880	68.493	2.0
14	1	0	8	1.34010	70.172	4.0
15	2	0	3	1.29830	72.785	6.0
16	1	1	6	1.25130	75.991	4.0
17	0	0	10	1.22950	77.587	2.0
18	1	0	9	1.22240	78.123	2.0
19	2	0	5	1.19600	80.191	4.0
20	1	1	8	1.10150	88.745	6.0
21	1	0	11	1.03470	96.227	6.0
22	2	0	8	1.02150	97.891	2.0
23	2	1	3	1.00290	100.362	6.0
24	1	1	10	0.97040	105.083	2.0
25	2	1	5	0.95340	107.792	4.0
26	3	0	2	0.90240	117.213	2.0
27	1	0	13	0.89390	119.022	4.0
28	0	0	14	0.87830	122.573	2.0
29	2	0	11	0.86580	125.670	2.0
30	1	0	14	0.83620	134.201	1.0

Name and formula

Reference code: 04-007-2356

Mineral name: Tugarinovite, syn
Compound name: Molybdenum Oxide
Common name: molybdenum(IV) oxide
PDF index name: Molybdenum Oxide

Empirical formula: MoO_2
Chemical formula: MoO_2

Crystallographic parameters

Crystal system: Monoclinic
Space group: P21
Space group number: 4

a (Å):   5.6100
b (Å):   4.8430
c (Å):   5.5260
Alpha (°):   90.0000
Beta (°):   119.6200
Gamma (°):   90.0000

Measured density (g/cm^3):   6.44
Volume of cell (10^6 pm^3):   130.52

Peak list

No.	h	k	l	d [Å]	2Theta[deg]	I [%]
1	0	0	1	4.80388	18.454	1.5
2	-1	0	1	4.80388	18.454	1.5
3	1	1	0	3.43644	25.907	7.4
4	0	1	1	3.41354	26.083	100.0
5	-1	1	1	3.41354	26.083	100.0
6	1	0	1	2.80467	31.882	1.7
7	-2	0	1	2.80467	31.882	1.7
8	2	0	0	2.43845	36.830	13.6
9	0	2	0	2.42389	37.059	31.0
10	1	1	1	2.42389	37.059	31.0
11	-1	1	2	2.40194	37.410	16.4
12	0	0	2	2.40194	37.410	16.4
13	2	1	0	2.17796	41.425	2.2
14	0	2	1	2.16307	41.723	1.0
15	-1	2	1	2.16307	41.723	1.0
16	0	1	2	2.15182	41.952	2.4
17	-2	1	2	2.15182	41.952	2.4
18	2	0	1	1.83836	49.545	2.3
19	-3	0	1	1.83836	49.545	2.3
20	1	2	1	1.83288	49.703	2.0
21	-2	2	1	1.83288	49.703	2.0
22	-1	0	3	1.81066	50.355	0.1
23	-2	0	3	1.81066	50.355	0.1
24	-3	1	1	1.72058	53.192	10.9
25	2	2	0	1.71822	53.271	11.2
26	2	1	1	1.71822	53.271	11.2
27	-3	1	2	1.71193	53.482	3.5
28	0	2	2	1.70677	53.657	19.8
29	-2	2	2	1.70677	53.657	19.8
30	-1	1	3	1.69492	54.062	11.5
31	-2	1	3	1.69492	54.062	11.5
32	0	0	3	1.60129	57.508	0.4
33	3	1	0	1.54113	59.977	2.7
34	0	3	1	1.53051	60.437	6.0
35	-1	3	1	1.53051	60.437	6.0
36	-3	1	3	1.52269	60.780	5.3
37	2	2	1	1.46421	63.483	1.3
38	-3	2	1	1.46421	63.483	1.3
39	-1	2	3	1.45010	64.174	0.1
40	-2	2	3	1.45010	64.174	0.1
41	-4	0	2	1.40233	66.638	2.3
42	1	3	1	1.39851	66.844	6.3
43	-2	3	1	1.39851	66.844	6.3
44	-2	0	4	1.38150	67.777	2.7
45	3	0	1	1.35175	69.480	0.8
46	-4	0	1	1.35175	69.480	0.8
47	2	3	0	1.34700	69.760	0.2
48	-4	1	2	1.34700	69.760	0.2
49	0	3	2	1.34062	70.141	0.8
50	-4	0	3	1.34062	70.141	0.8
51	0	2	3	1.33567	70.439	0.4

52	-1	0	4	1.32850	70.877	0.2
53	-2	1	4	1.32850	70.877	0.2
54	3	1	1	1.30084	72.620	1.7
55	-4	1	1	1.30084	72.620	1.7
56	1	1	3	1.28965	73.353	2.3
57	-3	1	4	1.28242	73.834	0.1
58	-1	1	4	1.28117	73.918	0.2
59	4	0	0	1.21922	78.366	0.3
60	-4	2	2	1.21368	78.793	2.5
61	-3	3	1	1.21368	78.793	2.5
62	2	2	2	1.21194	78.928	1.4
63	1	3	2	1.21075	79.021	2.1
64	0	4	0	1.21075	79.021	2.1
65	-1	3	3	1.20457	79.506	1.8
66	-2	3	3	1.20457	79.506	1.8
67	-4	0	4	1.20302	79.629	1.6
68	-2	2	4	1.19995	79.874	2.0
69	0	0	4	1.19995	79.874	2.0
70	3	2	1	1.18030	81.480	1.1

Bibliography

[1] T Bak et al. "Photo-electrochemical hydrogen generation from water using solar energy. Materials-related aspects". In: *International journal of hydrogen energy* 27.10 (2002), pp. 991–1022.

[2] T. Bak et al. "Photo-electrochemical properties of the TiO 2-Pt system in aqueous solutions". In: *International Journal of Hydrogen Energy* 27.1 (2002), pp. 19–26.

[3] Sivacarendran Balendhran et al. "Two dimensional molybdenum trioxide and dichalcogenides". In: *Advanced Functional Materials* 23.32 (2013), pp. 3952–3970.

[4] Allen J. Bard et al. "The concept of Fermi level pinning at semiconductor/liquid junctions. Consequences for energy conversion efficiency and selection of useful solution redox couples in solar devices". In: *Journal of the American Chemical Society* 102.11 (1980), pp. 3671–3677.

[5] Alexandre-Edmond Becquerel. "Mémoire sur les effets électriques produits sous l'influence des rayons solaires". In: *Comptes Rendus* 9.567 (1839), p. 1839.

[6] Jesse D. Benck et al. "Catalyzing the Hydrogen Evolution Reaction (HER) with Molybdenum Sulfide Nanomaterials". In: *ACS Catalysis* 4.11 (2014), pp. 3957–3971.

[7] Jesse D Benck et al. "Catalyzing the Hydrogen Evolution Reaction (HER) with Molybdenum Sulfide Nanomaterials". In: *ACS Catalysis* 4.11 (2014), pp. 3957–3971.

[8] Zhebo Chen, Arnold J. Forman, and Thomas F. Jaramillo. "Bridging the gap between bulk and nanostructured photoelectrodes: The impact of surface states on the electrocatalytic and photoelectrochemical properties of MoS2". In: *The Journal of Physical Chemistry C* 117.19 (2013), pp. 9713–9722.

[9] Zhebo Chen et al. "Core shell MoO3 MoS2 nanowires for hydrogen evolution: A functional design for electrocatalytic materials". In: *Nano letters* 11.10 (2011), pp. 4168–4175.

[10] BE Conway and BV Tilak. "Interfacial processes involving electrocatalytic evolution and oxidation of H 2, and the role of chemisorbed H". In: *Electrochimica Acta* 47.22 (2002), pp. 3571–3594.

[11] George W. Crabtree, Mildred S. Dresselhaus, and Michelle V. Buchanan. "The hydrogen economy". In: *Physics Today* 57.12 (2004), pp. 39–44.

[12] MR Gennero de Chialvo and AC Chialvo. "Hydrogen evolution reaction: Analysis of the Volmer-Heyrovsky-Tafel mechanism with a generalized adsorption model". In: *Journal of Electroanalytical Chemistry* 372.1 (1994), pp. 209–223.

[13] Raymond N. Dominey et al. "Improvement of photoelectrochemical hydrogen generation by surface modification of p-type silicon semiconductor photocathodes". In: *Journal of the American Chemical Society* 104.2 (1982), pp. 467–482.

[14] Dumitru Dumcenco et al. "Large-Area Epitaxial Monolayer MoS2". In: *ACS nano* 9.4 (2015), pp. 4611–4620.

[15] Shalom E. Aharon and Adam Heller. "Efficient pInP (Rh H alloy) and pInP (Re H alloy) hydrogen evolving photocathodes". In: *Journal of the Electrochemical Society* 129.12 (1982), pp. 2865–2866.

[16] "Effect of the pn junction engineering on Si microwire array solar cells". In: *physica status solidi (a)* 209.8 (2012), pp. 1588–1591.

[17] A. Fujishima and K. Honda. "TiO2 photoelectrochemistry and photocatalysis". In: *Nature* 238.5358 (1972), pp. 37–38.

[18] K. Gelderman, L. Lee, and SW Donne. "Flat-band potential of a semiconductor: using the Mott?Schottky equation". In: *Journal of chemical education* 84.4 (2007), p. 685.

[19] Michael Grätzel. "Photoelectrochemical cells". In: *Nature* 414.6861 (2001), pp. 338–344.

[20] Craig A. Grimes, Oomman K. Varghese, and Sudhir Ranjan. *Hydrogen generation by water splitting*. Springer, 2008.

[21] Thomas W. Hamann et al. "Measurement of the driving force dependence of interfacial charge-transfer rate constants in response to pH changes at n-ZnO/H 2 O interfaces". In: *Chemical Physics* 326.1 (2006), pp. 15–23.

[22] Berit Hinnemann et al. "Biomimetic hydrogen evolution: MoS2 nanoparticles as catalyst for hydrogen evolution". In: *Journal of the American Chemical Society* 127.15 (2005), pp. 5308–5309.

[23] T. F. Jaramillo et al. "Identification of active edge sites for electrochemical H2 evolution from MoS2 nanocatalysts". In: *Science (New York, N.Y.)* 317.5834 (2007), pp. 100–102.

[24] Jakob Kibsgaard et al. "Engineering the surface structure of MoS2 to preferentially expose active edge sites for electrocatalysis". In: *Nature materials* 11.11 (2012), pp. 963–969.

[25] Desheng Kong et al. "Synthesis of MoS2 and MoSe2 films with vertically aligned layers". In: *Nano letters* 13.3 (2013), pp. 1341–1347.

[26] Changgu Lee et al. "Anomalous lattice vibrations of single-and few-layer MoS2". In: *ACS nano* 4.5 (2010), pp. 2695–2700.

[27] Nathan S. Lewis. "A Quantitative Investigation of the Open?Circuit Photovoltage at the Semiconductor/Liquid Interface". In: *Journal of the Electrochemical Society* 131.11 (1984), pp. 2496–2503.

[28] Carlos G Morales Guio, Lucas Alexandre Stern, and Xile Hu. "Nanostructured hydrotreating catalysts for electrochemical hydrogen evolution". In: *Chemical Society Reviews* 43.18 (2014), pp. 6555–6569.

[29] Arthur J. Nozik and Rudiger Memming. "Physical chemistry of semiconductor-liquid interfaces". In: *The Journal of physical chemistry* 100.31 (1996), pp. 13061–13078.

[30] Branimir Radisavljevic et al. *Single-layer MoS2 transistors*. Tech. rep. 6. Nature Publishing Group, 2011, pp. 147–150.

[31] Krishnan Rajeshwar. "Fundamentals of semiconductor electrochemistry and photoelectrochemistry". In: *Encyclopedia of electrochemistry* (2002).

[32] Egill Skulason et al. "Modeling the electrochemical hydrogen oxidation and evolution reactions on the basis of density functional theory calculations". In: *The Journal of Physical Chemistry C* 114.42 (2010), pp. 18182–18197.

[33] Andrea Splendiani et al. "Emerging photoluminescence in monolayer MoS2". In: *Nano letters* 10.4 (2010), pp. 1271–1275.

[34] Simon M. Sze and Kwok K. Ng. *Physics of semiconductor devices*. John Wiley and Sons, 2006.

[35] John Turner et al. "Renewable hydrogen production". In: *International Journal of Energy Research* 32.5 (2008), pp. 379–407.

[36] Michael G. Walter et al. "Solar water splitting cells". In: *Chemical reviews* 110.11 (2010), pp. 6446–6473.

[37] H. Wang et al. "Electrochemical tuning of vertically aligned MoS2 nanofilms and its application in improving hydrogen evolution reaction". In: *Proceedings of the National Academy of Sciences of the United States of America* 110.49 (2013), pp. 19701–19706.

[38] Qing Hua Wang et al. "Electronics and optoelectronics of two-dimensional transition metal dichalcogenides". In: *Nature nanotechnology* 7.11 (2012), pp. 699–712.

[39]   Shanshan Wang et al. "Shape Evolution of Monolayer MoS2 Crystals Grown by Chemical Vapor Deposition". In: *Chemistry of Materials* 26.22 (2014), pp. 6371–6379.

[40]   Kübra Yasaroglu. *etude de semiconductores nanostructurès pour la photoèlectolisè de l'eau*. 2014.